# Sea-State-Dependent Sea Spray and Air–Sea Heat Fluxes in Tropical Cyclones: A New Parameterization for Fully Coupled Atmosphere–Wave–Ocean Models

BENJAMIN W. BARR,[a] SHUYI S. CHEN,[a] AND CHRISTOPHER W. FAIRALL[b]

[a] *University of Washington, Seattle, Washington*
[b] *Physical Sciences Laboratory, National Oceanic and Atmospheric Association, Boulder, Colorado*

(Manuscript received 1 June 2022, in final form 15 October 2022)

ABSTRACT: Air–sea exchange in high winds is one of the most important but poorly represented processes in tropical cyclone (TC) prediction models. Effects of sea spray on air–sea heat fluxes in TCs are particularly difficult to model due to complex sea states and lack of observations in extreme wind and wave conditions. This study introduces a new sea-state-dependent air–sea heat flux parameterization with spray, which is developed using the Unified Wave Interface–Coupled Model (UWIN-CM). Impacts of spray on air–sea heat fluxes are investigated across a wide range of winds, waves, and atmospheric and ocean conditions in five TCs of various sizes and intensities. Spray generation with variable size distribution is explicitly represented by surface wave properties such as wave dissipation, significant wave height, and dominant phase speed, which may be uncorrelated with local winds. The sea-state-dependent spray mass flux is substantially different than a wind-dependent flux, especially when wave shoaling occurs with enhanced wave dissipation near the coast during TC landfall. Spray increases the air–sea enthalpy flux near the radius of maximum wind (RMW) by approximately 5%–20% when mean 10-m wind speed at the RMW reaches 40–50 m $s^{-1}$. These values can be amplified significantly by coastal wave shoaling. Spray latent heat fluxes may be dampened in the eyewall due to high saturation ratio, and they consistently produce a moistening and cooling effect outside the eyewall. Spray strongly modifies the total sensible heat flux and can cause either a warming or cooling effect at the RMW depending on eyewall saturation ratio.

SIGNIFICANCE STATEMENT: Fluxes of heat and moisture from the ocean to the atmosphere are important for hurricane intensification, but the impact of sea spray generated by breaking waves on these fluxes is not well understood. We develop a new model for heat fluxes with spray that accounts for how waves control spray, and we apply this model to a set of five simulated hurricanes to better understand the broad range of ways that spray impacts heat fluxes in high wind conditions. We find that spray significantly affects heat fluxes in hurricanes and that impacts are strongly controlled by waves, which are not always correlated to winds. This research improves our understanding of how spray affects heat fluxes in hurricanes and provides a foundation for future studies investigating sea spray and its impacts on high-impact weather systems.

KEYWORDS: Atmosphere-ocean interaction; Hurricanes/typhoons; Wind waves; Surface fluxes; Coupled models; Parameterization

## 1. Introduction

Air–sea heat fluxes are widely recognized to play a key role in tropical cyclone (TC) intensification (e.g., Shapiro and Willoughby 1982; Emanuel 1995), but they are difficult to observe in high wind conditions (i.e., 10-m wind speed $U_{10} \gtrsim 20$ m $s^{-1}$) (Zhang et al. 2008; Drennan et al. 2007) and are not well-represented in models (Sroka and Emanuel 2021a). The existing bulk algorithms for air–sea sensible and latent heat fluxes (SHFs and LHFs) represent vertical transport of heat and moisture by turbulent eddies using Monin–Obukhov (MO) similarity theory (Monin and Obukhov 1954) but do not address the important contribution of sea spray (e.g., Fairall et al. 2003). In high winds, sea spray ejected from breaking waves introduces a new avenue for heat transfer, i.e., cooling and evaporation of droplets (Veron 2015; Richter and Veron 2016), which is thought to substantially modify air–sea heat fluxes (Andreas 1992; Fairall et al. 1994, hereafter F94; Andreas and Emanuel 2001; Zhao et al. 2006; Bao et al. 2011; C. W. Fairall et al. 2014, unpublished report; Mueller and Veron 2014b; Richter and Stern 2014; Andreas et al. 2015; Troitskaya et al. 2018b; He et al. 2018; Sroka and Emanuel 2021b) in ways that promote TC intensification (Kepert et al. 1999; Bao et al. 2000; Wang et al. 2001; Cheng et al. 2012; Zhang et al. 2017; Garg et al. 2018; Prakash et al. 2019; Xu et al. 2021b).

Understanding and modeling of spray heat transfer has progressed in recent decades, but the crucial control of spray generation and heat transfer in high winds by the physics of breaking waves and wave dissipation related to sea state remains largely unresolved. Pioneering work on spray production (e.g., Monahan et al. 1986), which largely did not address high winds, recognized the importance of waves, whitecaps, air entrainment, and bubble bursting in spray production, but these effects were generally parameterized in terms of $U_{10}$. This work gave rise to the most commonly used model for spray generation (F94), which prescribes total spray mass flux using a $U_{10}$-based whitecap fraction and defines a universal (i.e., not wind- or sea-state-dependent) droplet size distribution based on observations. Recent laboratory studies (Veron

*Corresponding author*: Benjamin Barr, bwbarr@uw.edu

DOI: 10.1175/JAS-D-22-0126.1

et al. 2012; Troitskaya et al. 2017, 2018a; Ortiz-Suslow et al. 2016, hereafter OS16; Bruch et al. 2021) have illuminated the complex dynamics of spray generation by breaking waves in high winds, demonstrating both control of spray generation by wave processes and the droplet distribution's ability to change with conditions. A number of wave-based spray generation models have recently been proposed; some of these allow the droplet size distribution to vary (Fairall et al. 2009; Mueller and Veron 2009; Troitskaya et al. 2018a), while others do not (Zhao et al. 2006; Zhang et al. 2017; Xu et al. 2021a). These models have large uncertainties and stand to benefit from further development and calibration based on ever-improving observational datasets.

In addition to their direct role in spray generation, the manner in which dynamic, spatially varying wave fields in TCs modulate spray heat fluxes is essentially unknown. Sea states in TCs are generally understood as a superposition of local wind seas and swell propagating from the high-wind region of the storm. Wave fields in translating TCs are highly asymmetric, with resonant growth of swell aligned with winds on the right side producing the highest and longest waves in the front-right (FR) quadrant (Wright et al. 2001; Chen et al. 2013; Zhang and Oey 2019; Tamizi and Young 2020; Northern Hemisphere convention used throughout). On the left side of the storm, unaligned swell and wind-sea produce smaller, shorter waves (Chen and Curcic 2016). Open ocean patterns are disrupted during storm landfall by processes such as wave shoaling, refraction, and offshore flow over very short fetch (Chen and Curcic 2016). In deep water, waves break by "spilling" and release about one-third of their energy to dissipation; when waves shoal in shallow water, they break by "plunging" and dissipate energy much more quickly (Donelan et al. 2012).

The effects of sea state on spray generation and air–sea heat fluxes with spray have not been systematically investigated across a wide range of conditions in TCs. In fact, control of heat fluxes with spray by storm-scale surface thermodynamics is also largely unknown, since previous studies of air–sea heat fluxes with spray (e.g., Andreas 1992; Mueller and Veron 2014b; Andreas et al. 2015; Troitskaya et al. 2018b) typically evaluate a limited set of test cases. Parametric variations that have been performed suggest that spray effects depend strongly on near-surface thermodynamics. For example, Andreas et al. (2015) varied relative humidity from 75% to 100% at $U_{10} = 25$ m s$^{-1}$ and found that the spray latent heat flux varied from over 350 W m$^{-2}$ to below 0 W m$^{-2}$. Without knowledge of storm-scale variations in surface conditions to put these values in context, it is difficult to evaluate the true impact of spray on air–sea heat fluxes.

This study aims to better understand and improve model representation of sea-state-dependent air–sea heat fluxes with spray by developing and testing a new parameterization across a wide range of TC conditions found in model output of fully coupled atmosphere–wave–ocean (AWO) TC simulations, allowing us to characterize control of heat fluxes with spray by sea state and surface thermodynamics. We focus herein on characterizing air–sea heat fluxes with spray in complex TC conditions by exercising our new parameterization on output from coupled AWO model simulations of five TCs with various intensities; effects of spray-mediated air–sea heat fluxes on TC structure and intensity in the fully coupled model will be addressed in a future study. The coupled model and new spray heat flux parameterization are described in sections 2 and 3, respectively. In section 4, we characterize sea-state-based spray generation and heat fluxes in TCs, starting first with a single simulation of a translating TC in the open ocean and then expanding our study to explore spray impacts on heat fluxes across a diverse set of five TC simulations. In section 5, we summarize our conclusions.

## 2. Coupled model

The coupled model used for the TC simulations in this study is the Unified Wave Interface–Coupled Model (UWIN-CM), a fully coupled AWO model (Chen et al. 2013; Chen and Curcic 2016). The atmospheric component of UWIN-CM is the Weather Research and Forecasting Model (WRF-ARW) (Skamarock et al. 2008), v3.9, which was run with nested domains of 12-, 4-, and 1.3-km horizontal resolution and 44 vertical levels. Inner nests were set as vortex-following where appropriate. The surface-layer scheme is based on MO theory with scalar roughness lengths per Garratt (1992), and the boundary layer parameterization is the Yonsei University scheme (Hong et al. 2006). The surface wave component of UWIN-CM is the University of Miami Wave Model (UMWM) (Donelan et al. 2012), v2.1, which was run with 4-km horizontal resolution, 32 or 36 directional bins, and 37 frequency bins from 0.0313 to 2.0 Hz. The ocean component of UWIN-CM is the Hybrid Coordinate Ocean Model (HYCOM) (Wallcraft et al. 2009), v2.2.99, which was run with 0.04° (~4-km) horizontal resolution and 41 or 32 vertical levels.

We performed simulations for five TCs. These are Hurricanes Harvey (2017), Florence (2018), Michael (2018), and Dorian (2019) and Typhoon Fanapi (2010). The simulations were initialized and concluded at 0000 UTC 24 August and 1200 UTC 26 August 2017 for Harvey, 0000 UTC 10 September and 1200 UTC 14 September 2018 for Florence, 0600 UTC 8 October and 0000 UTC 11 October 2018 for Michael, 0000 UTC 28 August and 0000 UTC 6 September 2019 for Dorian, and 0000 UTC 15 September and 0000 UTC 20 September 2010 for Fanapi. Initial and boundary conditions (ICs and BCs) for WRF come from European Centre for Medium-Range Weather Forecasts ERA5 0.25° data (Michael, Dorian) and National Centers for Environmental Prediction Global Forecasting System 0.25° forecast fields (Harvey, Florence, Fanapi). ICs and BCs for HYCOM come from 1/12° Global Ocean Forecast System, version 3.0 and 3.1, global HYCOM model analysis (all TCs). Simulations for Florence, Michael, Dorian, and Fanapi were initialized using a relocated vortex (Lin et al. 2018). Because of the long duration of the Hurricane Dorian simulation, it was necessary to reinitialize the large-scale atmosphere at 1200 UTC 30 August 2019 to improve the environmental steering flow affecting the storm track along the U.S. Atlantic coast. The simulation of Hurricane Michael underestimated the observed rapid intensification prior to landfall, which is a well-known issue in TC forecasting (e.g. Cangialosi 2020). To mitigate

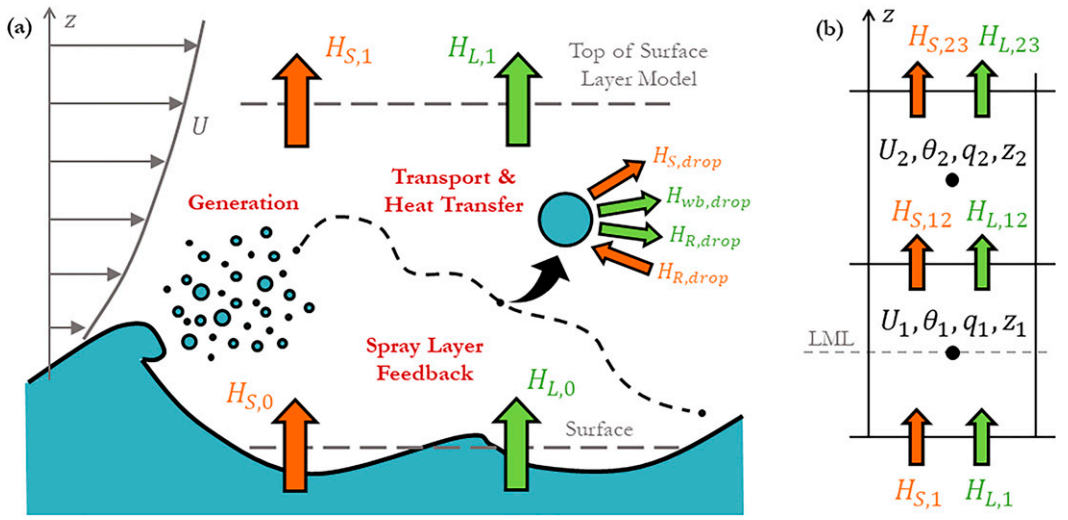


FIG. 1. (a) Fluxes and physical processes addressed by our new air–sea heat flux parameterization with spray. Fluxes $H_{S,\mathrm{drop}}$, $H_{\mathrm{wb,drop}}$, and $H_{R,\mathrm{drop}}$ are the droplet-specific SHF, heat flux due to temperature change from air temperature $T$ to salt-adjusted wet-bulb temperature $T_{\mathrm{wb}}$, and heat flux due to size change, respectively. These heat fluxes are integrated over the sea spray generation function to obtain $H_{S,\mathrm{spr}}$, $H_{\mathrm{wb,spr}}$, and $H_{R,\mathrm{spr}}$, which are defined in the text. $H_{S,0}$ and $H_{L,0}$ are the SHF and LHF at the surface in the presence of spray, and $H_{S,1}$ and $H_{L,1}$ are the total SHF and LHF with spray produced by the parameterization. (b) Fluxes and variables for sample grid cells in the lowest two layers of the WRF Model. Subscripts 1 and 2 on variables $U$, $\theta$, $q$, and $z$ indicate values at the cell centers (i.e., mass points) of the lowest and second-lowest layers of cells, respectively. Fluxes $H_{S,12}$ and $H_{L,12}$ are the vertical SHF and LHF from the lowest to second-lowest layers, and fluxes $H_{S,23}$ and $H_{L,23}$ are the vertical SHF and LHF from the second-lowest to third-lowest layers.

potential error in the ocean initial condition, we decoupled feedback of sea surface temperature from the ocean to the atmosphere after 2100 UTC 8 October 2018, which produced a realistic intensification.

## 3. Air–sea heat flux parameterization with spray

The new air–sea heat flux parameterization presented in this study predicts the total SHF and LHF ($H_{S,1}$ and $H_{L,1}$, respectively) by modeling the physical processes of spray generation, spray transport and heat transfer to the near-surface flow, and feedback between spray heat fluxes and the near-surface environment (Fig. 1a). Spray generation is sea-state based and is adapted from Fairall et al. (2009); we update several physical assumptions and scalings of this earlier model and calibrate it using available field and laboratory observations. Spray heat fluxes are calculated using radius-specific time scales for droplet cooling, evaporation, and settling, as is commonly done (Andreas 1989, 1990, 1992, 2005; F94; Andreas and DeCosmo 1999). Near-surface feedback is addressed by modeling the vertical divergence of turbulent heat fluxes due to spray within a MO model of the surface layer, building on earlier work (Andreas et al. 1995; Andreas 2004; Bao et al. 2011; C. W. Fairall et al. 2014, unpublished report; Mueller and Veron 2014b).

Inputs to the parameterization are the wave energy dissipation flux ($\varepsilon$), significant wave height ($H_S$), dominant phase speed ($C_{p,d}$), mean squared wave slope ($s_m$), and friction velocity ($u_*$), which come from the wave model; ocean surface temperature ($T_0$), which comes from the ocean model; and surface pressure ($P_0$) plus horizontal wind speed, potential temperature, specific humidity, and height at the lowest model mass level (LML) of the atmospheric model ($U_1$, $\theta_1$, $q_1$, and $z_1$, respectively). In WRF-ARW, model mass points are at gridcell centers, so height $z$ (from geopotential) and components of horizontal wind speed $U$ must be vertically and horizontally unstaggered, respectively, to obtain values at mass points. With $U_1$, $\theta_1$, $q_1$, and $z_1$ defined at the LML, the parameterization produces $H_{S,1}$ and $H_{L,1}$, which are applied at the bottom boundary of the lowest layer of cells and used to calculate the vertical flux divergence at the LML during the WRF Model integration (Fig. 1b).

### a. Spray generation

We define generation of spray spume droplets using a sea-state-based sea spray generation function (SSGF) that assumes that droplets are formed by converting a small portion of the turbulent kinetic energy (TKE) within breaking wave crests into surface potential energy of spray droplets (Fairall et al. 2009). Note that we neglect film and jet droplets in our model as these are produced by a fundamentally different wave process (i.e., bursting of entrained bubbles) and are broadly considered to have minimal impact on spray mass and heat fluxes (e.g., Andreas 1992). After formation, a fraction of the produced droplet population is ejected from the wave crest and enters the surface flow, with the probability of

ejection determined by the ballistics of the droplets at the wave crest. The SSGF in terms of mass, $dm/dr_0$, is

$$\frac{dm}{dr_0} = \frac{C_1 f_s \rho_{sw} \tilde{\varepsilon} r_0 W_{SS}}{3\sigma_{surf}} \exp\left[-\frac{3}{2} C_2 \alpha_k \left(\frac{\pi\eta_k}{r_0}\right)^{4/3}\right] \times \frac{1}{2}\left[1 + \mathrm{erf}\left(\frac{U_{h,rel} - \frac{v_g}{C_3 s_m}}{C_4 \sigma_h} - C_5\right)\right]. \quad (1)$$

The factors on the right to the left and right of the × sign are the size distribution of droplets produced from TKE and the droplet ejection probability, respectively; $C_1$ through $C_5$ and $f_s$ are model coefficients, $\rho_{sw}$ is the density of seawater, $\tilde{\varepsilon}$ is the volumetric kinematic dissipation rate under actively breaking whitecaps [see Brumer et al. (2017) for an observationally driven treatment of whitecaps in high winds], $r_0$ is the droplet radius at formation, $W_{SS}$ is a sea-state-based estimate of the actively breaking whitecap fraction, $\sigma_{surf}$ is the ratio of surface tension to density for water, $\alpha_k$ is the Kolmogorov constant, and $\eta_k$ is the Kolmogorov microscale on the water side based on $\tilde{\varepsilon}$. $v_g$ is the droplet gravitational settling velocity, $s_m$ is the mean squared wave slope, $\sigma_h$ is the standard deviation of the horizontal turbulent wind speed at a gust height $h_{gust}$, and $U_{h,rel} = U_h - 0.8C_{p,d}$ is the ejected droplet velocity relative to the moving wave crest, with $U_h$ as the horizontal wind speed at $h_{gust}$ and the factor of 0.8 per Banner et al. (2014). We define $\tilde{\varepsilon}$ based on measurements and scaling from Sutherland and Melville (2015) as follows:

$$\tilde{\varepsilon} = \frac{C_{diss}\varepsilon}{H_S \rho_{sw} W_{SS}}. \quad (2)$$

Here $C_{diss}$ is a nondimensional constant that we select as $10^2$ based on Fig. 11 of their paper. Note that substituting (2) into (1) eliminates $W_{SS}$ from the multiplicative group preceding the exponential but that the sea-state-based SSGF still depends on $W_{SS}$ through $\eta_k$ (see appendix).

We compare our sea-state-based SSGF to an updated wind-based model based on F94, defined as

$$\frac{dm}{dr_0} = f_s W_{wi} \left(\frac{dm}{dr_0}\right)_{F94}. \quad (3)$$

Here $(dm/dr_0)_{F94}$ is the F94 droplet spectrum per unit whitecap [implemented according to Mueller and Veron (2014b), section 3c(2)] and $W_{wi}$ is a wind-based whitecap fraction parameterization.

Additional variable definitions and calibration of model coefficients are described in the appendix.

### b. Spray heat fluxes

#### 1) Spray heat fluxes due to temperature and size change

Detailed microphysical models (Andreas 1989, 1990, 1992) have shown that temperature change is roughly three orders of magnitude faster than size change for spume droplets, so that droplet cooling and evaporation processes are effectively decoupled. Spray droplet heat transfer may thus be approximated as 1) cooling/warming at constant $r_0$ from $T_0$ to the salt-adjusted wet-bulb temperature $T_{wb}$ of the air, followed by 2) evaporation/condensation at constant $T_{wb}$ to the droplet's equilibrium radius $r_{eq}$. Andreas (1989, 1990, 2005) approximated these processes as

$$T_{drop,f} = T_{wb} + (T_0 - T_{wb}) \exp\left(-\frac{\tau_f}{\tau_T}\right), \quad (4a)$$

$$r_f = r_{eq} + (r_0 - r_{eq}) \exp\left(-\frac{\tau_f}{\tau_R}\right), \quad (4b)$$

where $T_{drop,f}$ and $r_f$ are the droplet reentry temperature and radius, and $\tau_T$, $\tau_R$, and $\tau_f$ are characteristic time scales for droplet cooling, evaporation, and settling, respectively. From this, the spray heat fluxes into the near-surface flow due to temperature change ($H_{T,spr}$) and size change ($H_{R,spr}$) for the entire droplet population are

$$H_{T,spr} = \int c_{p,sw}(T_0 - T_{drop,f}) \frac{dm}{dr_0} dr_0, \quad (5a)$$

$$H_{R,spr} = \int L_v \left[1 - \left(\frac{r_f}{r_0}\right)^3\right] \frac{dm}{dr_0} dr_0, \quad (5b)$$

where $c_{p,sw}$ and $L_v$ are the specific heat capacity and latent heat of vaporization of seawater.

Similar to Fairall et al. (1990), we define $r_{eq}$ as

$$\frac{r_{eq}}{r_0} = \left[x_s\left(1 + \frac{\nu \Phi_s \frac{M_w}{M_s}}{1 - s}\right)\right]^{1/3}. \quad (6)$$

Here $\nu$ is the number of ions into which NaCl dissociates, $\Phi_s$ is the practical osmotic coefficient, $M_w$ and $M_s$ are molecular weights of water and salt, respectively, and $x_s$ is the mass fraction of salt in seawater. $s \approx q/q_{sat,0}(T)$ is the saturation ratio of air with specific humidity $q$, temperature $T$, and saturation specific humidity over a plane surface of pure water $q_{sat,0}(T)$.

We define the thermodynamic time scales $\tau_T$ and $\tau_R$ by scaling the classical equations for droplet temperature and radius change (e.g., Pruppacher and Klett 1997), obtaining

$$\tau_T = \frac{\rho_{sw} c_{p,sw} r_0^2}{3 k_a f_v}, \quad (7a)$$

$$\tau_R = \frac{\rho_{sw} r_0^2}{\rho_a D_a f_v q_{sat,0}(T) \beta (1 + y_0 - s)}. \quad (7b)$$

Here $k_a$ is the thermal conductivity of air, $f_v$ is the mean ventilation coefficient, $\rho_a$ is the air density, $D_a$ is the diffusivity of water vapor in air, and $\beta$ is the wet-bulb coefficient. The parameter $y_0$ accounts for the effect of salinity on saturation vapor pressure and equals −0.021 for typical surface seawater, so that air is saturated with respect to ejected spray droplets when $s = 0.979$.

We define $\tau_f$ in the usual way (Andreas 1992; F94; Andreas et al. 2015) as

$$\tau_f = \frac{\delta}{\upsilon_g}, \tag{8}$$

where $\delta$ is the spray-layer thickness. We choose $\delta = H_S$ based on Mueller and Veron (2014a); this study used detailed numerical simulations to suggest that the model $\tau_f = H_S/\upsilon_g$ may be incorrect by a factor between 0.5 and 2 but that $H_S$ is nonetheless the correct scaling for $\delta$. The value of $\delta$ is not allowed to be greater than $z_1$.

Finally, we define radius-specific heights for extracting ambient conditions ($T$, $q$) for spray calculations (i.e., specific heights for each droplet size that are appropriate for its thermodynamic time scales) following Peng and Richter (2019), which allows us to account for reheating and regrowth by condensation of small droplets as they reenter the ocean. More details on droplet reheating and regrowth and additional variable definitions are given in the appendix.

#### 2) Spray specific available energy and heat transfer efficiency

It is useful to regroup terms in $H_{T,\mathrm{spr}}$ and $H_{R,\mathrm{spr}}$ to clarify how conditions and processes govern fluxes. First, we define specific available energies $a_T$ and $a_R$ for $H_{T,\mathrm{spr}}$ and $H_{R,\mathrm{spr}}$, respectively, as

$$a_T = c_{p,\mathrm{sw}}(T_0 - T'_{\mathrm{wb,10N}}), \tag{9a}$$

$$a_R = L_v\left\{1 - \left[\left(\frac{r_{\mathrm{eq}}}{r_0}\right)'_{\mathrm{10N}}\right]^3\right\}. \tag{9b}$$

Here the subscript 10N indicates calculation using equivalent neutral 10-m variables, and the prime indicates that there are no spray feedback effects in the calculations. The specific available energies estimate the maximum energy extractable per unit mass of spray in terms of local conditions.

Next, we define $E_T(r_0)$ and $E_R(r_0)$ as dimensionless, radius-dependent droplet heat transfer efficiencies for temperature and size change, respectively:

$$E_T(r_0) = \frac{1}{a_T}c_{p,\mathrm{sw}}(T_0 - T_{\mathrm{drop},f}), \tag{10a}$$

$$E_R(r_0) = \frac{1}{a_R}L_v\left[1 - \left(\frac{r_f}{r_0}\right)^3\right]. \tag{10b}$$

Plugging (9) and (10) into (5) gives

$$H_{T,\mathrm{spr}} = a_T\int E_T\frac{dm}{dr_0}dr_0, \tag{11a}$$

$$H_{R,\mathrm{spr}} = a_R\int E_R\frac{dm}{dr_0}dr_0; \tag{11b}$$

$E_T$ and $E_R$ represent how well transport and thermodynamic processes transfer the available energy at each radius to the near-surface flow.

Next, we define $M_{\mathrm{spr}}$, the generated spray mass flux, as

$$M_{\mathrm{spr}} = \int\frac{dm}{dr_0}dr_0. \tag{12}$$

Finally, we define dimensionless mean spray heat transfer efficiencies $\overline{E}_T$ and $\overline{E}_R$ as

$$\overline{E}_T = \frac{1}{M_{\mathrm{spr}}}\int E_T\frac{dm}{dr_0}dr_0, \tag{13a}$$

$$\overline{E}_R = \frac{1}{M_{\mathrm{spr}}}\int E_R\frac{dm}{dr_0}dr_0; \tag{13b}$$

$\overline{E}_T$ and $\overline{E}_R$ weight $E_T$ and $E_R$ by the droplet sizes within the SSGF, providing a single number characterizing the efficiency of heat transfer for the droplet population as a whole. Plugging (13) into (11) gives

$$H_{T,\mathrm{spr}} = a_T\overline{E}_T M_{\mathrm{spr}}, \tag{14a}$$

$$H_{R,\mathrm{spr}} = a_R\overline{E}_R M_{\mathrm{spr}}. \tag{14b}$$

Thus, spray heat fluxes are determined by the mass of spray generated ($M_{\mathrm{spr}}$), the energy available within the spray ($a_T$ and $a_R$), and how well the near-surface flow extracts that energy from the droplet sizes present ($\overline{E}_T$ and $\overline{E}_R$).

#### 3) Spray sensible heat, latent heat, and enthalpy fluxes

The spray SHF and LHF, $H_{S,\mathrm{spr}}$ and $H_{L,\mathrm{spr}}$, respectively, are in general not equal to $H_{T,\mathrm{spr}}$ and $H_{R,\mathrm{spr}}$, respectively. This is because if $T$ is between $T_0$ and $T_{\mathrm{wb}}$, then the droplet temperature change from $T$ to $T_{\mathrm{wb}}$ exchanges droplet sensible heat for latent heat, producing a latent heat flux $H_{\mathrm{wb,spr}}$. The $H_{\mathrm{wb,spr}}$ portion of $H_{T,\mathrm{spr}}$ must be repartitioned with $H_{R,\mathrm{spr}}$ to calculate $H_{S,\mathrm{spr}}$ and $H_{L,\mathrm{spr}}$.

The energy for evaporation (or, if $s > 0.979$, from condensation) in $H_{R,\mathrm{spr}}$ is taken from (is rejected to) the sensible heat of the air and must be subtracted from (added to) $H_{S,\mathrm{spr}}$ to determine the net spray SHF, $H_{\mathrm{SN,spr}}$. Finally, the spray enthalpy flux $H_{K,\mathrm{spr}}$ is the sum of $H_{\mathrm{SN,spr}}$ and $H_{L,\mathrm{spr}}$, which is $H_{T,\mathrm{spr}}$, in accordance with Andreas and Emanuel (2001). These relationships are summarized as follows:

$$H_{S,\mathrm{spr}} = H_{T,\mathrm{spr}} - H_{\mathrm{wb,spr}}, \tag{15a}$$

$$H_{L,\mathrm{spr}} = H_{R,\mathrm{spr}} + H_{\mathrm{wb,spr}}, \tag{15b}$$

$$H_{\mathrm{SN,spr}} = H_{S,\mathrm{spr}} - H_{R,\mathrm{spr}}, \tag{15c}$$

$$H_{K,\mathrm{spr}} = H_{\mathrm{SN,spr}} + H_{L,\mathrm{spr}} = H_{T,\mathrm{spr}}. \tag{15d}$$

### c. *Air–sea heat fluxes with spray and near-surface feedback*

We calculate total heat fluxes with spray, including feedback, using a simple model for sensible and latent heat transfer

through a MO surface layer experiencing vertical divergence of turbulent heat fluxes due to spray. This model is derived in the appendix, and final expressions for heat fluxes and feedback are presented below.

Total SHF and LHF, including both spray and turbulent effects, are $H_{S,1}$ and $H_{L,1}$, respectively, defined as

$$H_{S,1} = H'_S + \gamma_S(H_{S,\mathrm{spr}} - H_{R,\mathrm{spr}}), \tag{16a}$$

$$H_{L,1} = H'_L + \gamma_L H_{L,\mathrm{spr}}, \tag{16b}$$

$$\gamma_S = \frac{\ln\left(\frac{\delta}{z_{0t}}\right) - \Psi_{H,\delta} - 1 + \varphi_{H,\delta}}{\ln\left(\frac{z_1}{z_{0t}}\right) - \Psi_{H,1}}, \tag{16c}$$

$$\gamma_L = \frac{\ln\left(\frac{\delta}{z_{0q}}\right) - \Psi_{H,\delta} - 1 + \varphi_{H,\delta}}{\ln\left(\frac{z_1}{z_{0q}}\right) - \Psi_{H,1}}. \tag{16d}$$

Here $H'_S$ and $H'_L$ are the turbulent interfacial SHF and LHF without spray, respectively, which are

$$H'_S = \frac{\rho_a c_{p,a}\kappa u_*(\theta_0 - \theta_1)}{\ln\left(\frac{z_1}{z_{0t}}\right) - \Psi_{H,1}}, \tag{17a}$$

$$H'_L = \frac{\rho_a L_v \kappa u_*(q_0 - q_1)}{\ln\left(\frac{z_1}{z_{0q}}\right) - \Psi_{H,1}}; \tag{17b}$$

$z_{0t}$ and $z_{0q}$ are thermal and moisture roughness lengths (Garratt 1992), $\Psi_H$ is the traditional integrated stability function for heat, and $\varphi_H$ is a new term that is the analog of $\Psi_H$ for a layer with volumetric heating. $c_{p,a}$ is the specific heat capacity of air, $\kappa$ is the von Kármán constant, and $\theta$ is potential temperature. Subscripts 0, $\delta$, and 1 indicate that variables or functions are evaluated at the surface, height $\delta$, and LML, respectively. $\gamma_S$ and $\gamma_L$ are feedback coefficients that address the "geometric" resistance to spray heat fluxes through the surface layer. For realistic TC conditions (i.e., $\Psi_{H,\delta}$, $\Psi_{H,1}$, and $\varphi_{H,\delta}$ are small compared to the other terms), $\gamma_S$ and $\gamma_L$ are always less than 1.0.

In addition to the effects of $\gamma_S$ and $\gamma_L$, feedback modifies $H_{S,\mathrm{spr}}$, $H_{R,\mathrm{spr}}$, and $H_{L,\mathrm{spr}}$ directly by changing the vertical $\theta$ and $q$ profiles within the spray layer. We account for this by iteratively calculating spray heat fluxes (15) and modified profiles [(A11) in the appendix] until they converge. The feedback effects between spray heat fluxes and vertical profiles are expressed by feedback coefficients $\alpha_S$, $\beta_S$, and $\beta_L$ as follows:

$$\alpha_S = \frac{H_{S,\mathrm{spr}}}{H'_{S,\mathrm{spr}}}, \tag{18a}$$

$$\beta_S = \frac{H_{R,\mathrm{spr}}}{H'_{R,\mathrm{spr}}}, \tag{18b}$$

$$\beta_L = \frac{H_{L,\mathrm{spr}}}{H'_{L,\mathrm{spr}}}. \tag{18c}$$

Here primed and nonprimed fluxes are calculated without and with spray modifications to vertical profiles, respectively.

Finally, we define 10-m neutral transfer coefficients for sensible heat ($C_{h,10N}$), latent heat ($C_{q,10N}$), and enthalpy ($C_{k,10N}$) below. Note that these definitions are based on the total fluxes $H_{S,1}$ and $H_{L,1}$ and apply to cases both with and without spray (in the latter case, $H_{S,1} = H'_S$ and $H_{L,1} = H'_L$):

$$C_{h,10N} = \frac{H_{S,1}}{\rho_a c_{p,a} U_{10N}(T_0 - T'_{10N})}, \tag{19a}$$

$$C_{q,10N} = \frac{H_{L,1}}{\rho_a L_v U_{10N}(q_0 - q'_{10N})}, \tag{19b}$$

$$C_{k,10N} = \frac{H_{S,1} + H_{L,1}}{\rho_a U_{10N}[c_{p,a}(T_0 - T'_{10N}) + L_v(q_0 - q'_{10N})]}. \tag{19c}$$

## 4. Sea-state-dependent heat fluxes with spray in tropical cyclones

### a. *Sample conditions from Hurricane Dorian (2019)*

We first characterize sea-state-dependent air–sea heat fluxes with spray using sample conditions from a UWIN-CM simulation of Hurricane Dorian (Avila et al. 2020). We select for analysis a 12-h period from 0000 to 1200 UTC 1 September (called Dor-O) when the storm is moving westward in the open Atlantic Ocean. Advanced Scatterometer (ASCAT) 0.25° satellite swath (Figa-Saldaña et al. 2002) surface wind speed and direction during this period (Fig. 2a) do not resolve the TC eyewall structure but indicate stronger wind speeds on the right side of the storm, reflecting established theory (e.g., Shapiro 1983). Surface wind speed estimates at 1 Hz derived from stepped frequency microwave radiometer (SFMR) measurements (Uhlhorn and Black 2003; Uhlhorn et al. 2007) at approximately the same time capture the high-wind eyewall structure. Daily gridded 9-km horizontal resolution Optimally Interpolated Sea Surface Temperature (OISST; Remote Sensing Systems 2017) shows a cold wake (Price 1981; Chen et al. 2007; Lee and Chen 2014) forming behind the storm, favoring the rear-right (RR) quadrant.

Simulated surface conditions are presented in Fig. 3, with storm-relative position in Fig. 3g expressed as the ratio of distance to storm center ($R$) to the radius of maximum azimuthally averaged 10-m wind speed (RMW). Surface winds (Figs. 3a,g) are strongest on the right side of the storm, as also seen in Fig. 2a, and wave dissipation flux (Figs. 3b,h) peaks in the FR quadrant. $H_S$ (Figs. 3c,i) is highest in the FR quadrant, agreeing with established patterns (e.g., Wright et al. 2001). The 10-m neutral, sprayless (i.e., not modified by spray feedback) air–sea temperature difference [$(T_0 - T'_{10N})$; Figs. 3d,j] increases with wind speed, and the 10-m neutral, sprayless air–sea specific humidity difference [$(q_0 - q'_{10N})$; Figs. 3e,k] decreases and then remains roughly constant as wind speed increases. The 10-m neutral, sprayless, salt-adjusted (i.e., equal to 1.0 when air is saturated with respected to the ejected saline droplets) saturation ratio [$(s'_{10N} - y_0)$; Figs. 3f,l] increases as wind speed increases

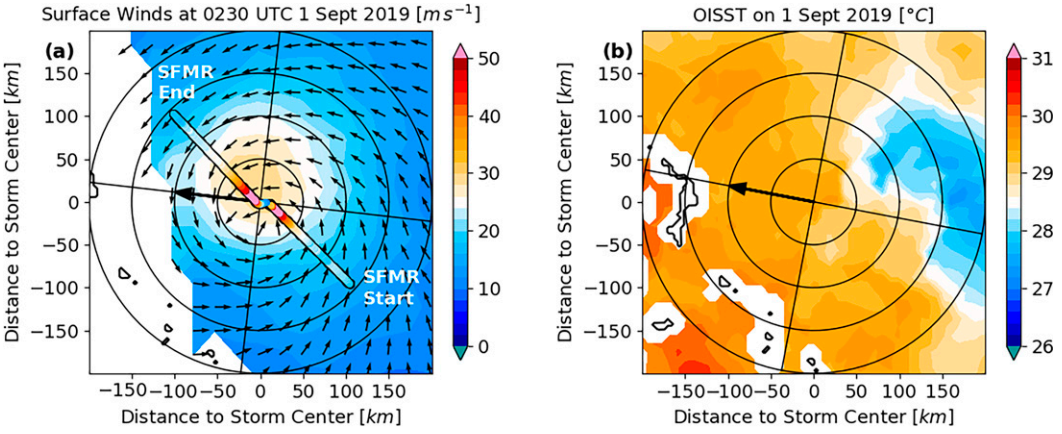


FIG. 2. (a) Storm-relative 0.25° Advanced Scatterometer (ASCAT) surface wind speed (colored field) and wind direction (unit vector field) from satellite overpass at approximately 0230 UTC 1 Sep 2019. Also shown is stepped-frequency microwave radiometer-estimated surface wind speed (colored line) from a flight segment from 0150 to 0236 UTC 1 Sep 2019. (b) Storm-relative 9-km Optimally Interpolated Sea Surface Temperature (OISST) on 1 Sep 2019. Observed storm centers at 0230 and 0600 UTC 1 Sep are used for (a) and (b), respectively.

and is close to 1.0 at the highest wind speeds. A cold wake is present in the RR quadrant as observed and is a major source of variability in the thermodynamic variables. Note that, in Figs. 3h–l, correlation of a particular variable with $U_{10}$ does not necessarily indicate causation. In the fully coupled AWO system, the variables in Fig. 3 are related through storm-scale air–sea–wave interactions that must be considered when determining causation among them. Finally, note that points in the eye disrupt trends for $U_{10} \lesssim 10\,\mathrm{m\,s^{-1}}$ in Fig. 3 and future figures.

### b. *Spray generation*

The wind-based SSGF maintains the same shape at all wind speeds, whereas the sea-state-based (SS-based) SSGF favors production of larger droplets at higher wind speeds (Figs. 4a,b), reflecting the growing ability of turbulent surface gusts to entrain large droplets at higher wind speeds. The SS-based model predicts approximately one order of magnitude higher (lower) spray mass flux than the wind-based model at 50 (20) m s$^{-1}$ (Figs. 4c,d), demonstrating that dissipation-based and whitecap-based models produce fundamentally different behavior. The SS-based results in Figs. 4c and 4d also have nonzero variance, reflecting the range of sea states that may occur at a given wind speed. The SS-based model predicts approximately one order of magnitude higher (lower) spray mass flux than the wind-based model at 1RMW (5RMW) (Figs. 4e,f).

### c. *Spray and air–sea heat fluxes*

$H_{T,\mathrm{spr}}$ and $H_{R,\mathrm{spr}}$ are controlled by the spray mass flux, specific available energies, and heat transfer efficiencies. $a_T$ decreases with increasing wind speed, levels off, and finally increases at the highest wind speeds (Fig. 5a). For reference, the quantity $c_{p,\mathrm{sw}}(T_0 - T'_{10\mathrm{N}})$, which is $a_T$ without the wet-bulb depression contribution, is also plotted. At low wind speeds, the wet-bulb contribution is substantial, but it decreases to become negligible at the highest wind speeds where $(s'_{10\mathrm{N}} - y_0)$ is high (Fig. 3l). $a_R$ (Fig. 5b), which is controlled by saturation ratio, is large at low wind speeds but plummets to near zero in the high-humidity eyewall.

Radius-specific heat transfer efficiencies $E_T$ and $E_R$ are shown in Figs. 5c and 5d without accounting for near-surface feedback effects, which makes the results independent of SSGF. Peak efficiency for $E_T$ occurs near $r_0 = 300\ \mu$m for all wind speeds, with larger droplets settling back to the ocean quickly and smaller droplets reheating to the ejection temperature upon reentry. Peak efficiency for $E_R$ occurs near $r_0 = 20\ \mu$m, with larger droplets settling quickly and smaller droplets regrowing by condensation as they pass through the near-saturated air at the ocean surface. $E_R$ generally decreases with wind speed due to the strong effect of $s$ on $\tau_R$ (7b). Thus, there is a double effect of high $s$ in dampening $H_{R,\mathrm{spr}}$; high $s$ limits both the potential for evaporation (through $a_R$) and the rate of evaporation (through $E_R$).

We note that our results in Figs. 5c and 5d are analogous to those of Mueller and Veron (2014a, their Figs. 9a and 10a). Our model reproduces many of the qualitative features of this much more detailed analysis, an encouraging indication that our model could be calibrated using such studies. Additionally, analysis not presented shows that neglecting regrowth of the smallest droplets by condensation as they reenter the ocean (i.e., the falloff of curves at the smallest radii in Fig. 5d) produces an error in the spray modifications to total heat fluxes that is generally below 2%, so the regrowth effect may be neglected.

The SSGF-weighted efficiencies $\overline{E}_T$ and $\overline{E}_R$ reveal that the SSGF shape has a significant impact on spray's ability to transfer heat. Since the wind-based SSGF shape does not change with wind speed, wind-based $\overline{E}_T$ (Fig. 5e) is mostly modulated by the ability of $H_s$ to increase the droplet residence time $\tau_f$ (cf. to Fig. 3i). For SS-based $\overline{E}_T$, the changing shape of the SSGF is also important, with efficiency dropping away from its peak near 30 m s$^{-1}$ as the SSGF favors smaller (larger) droplets at lower (higher) wind speeds. The peak of the wind-based

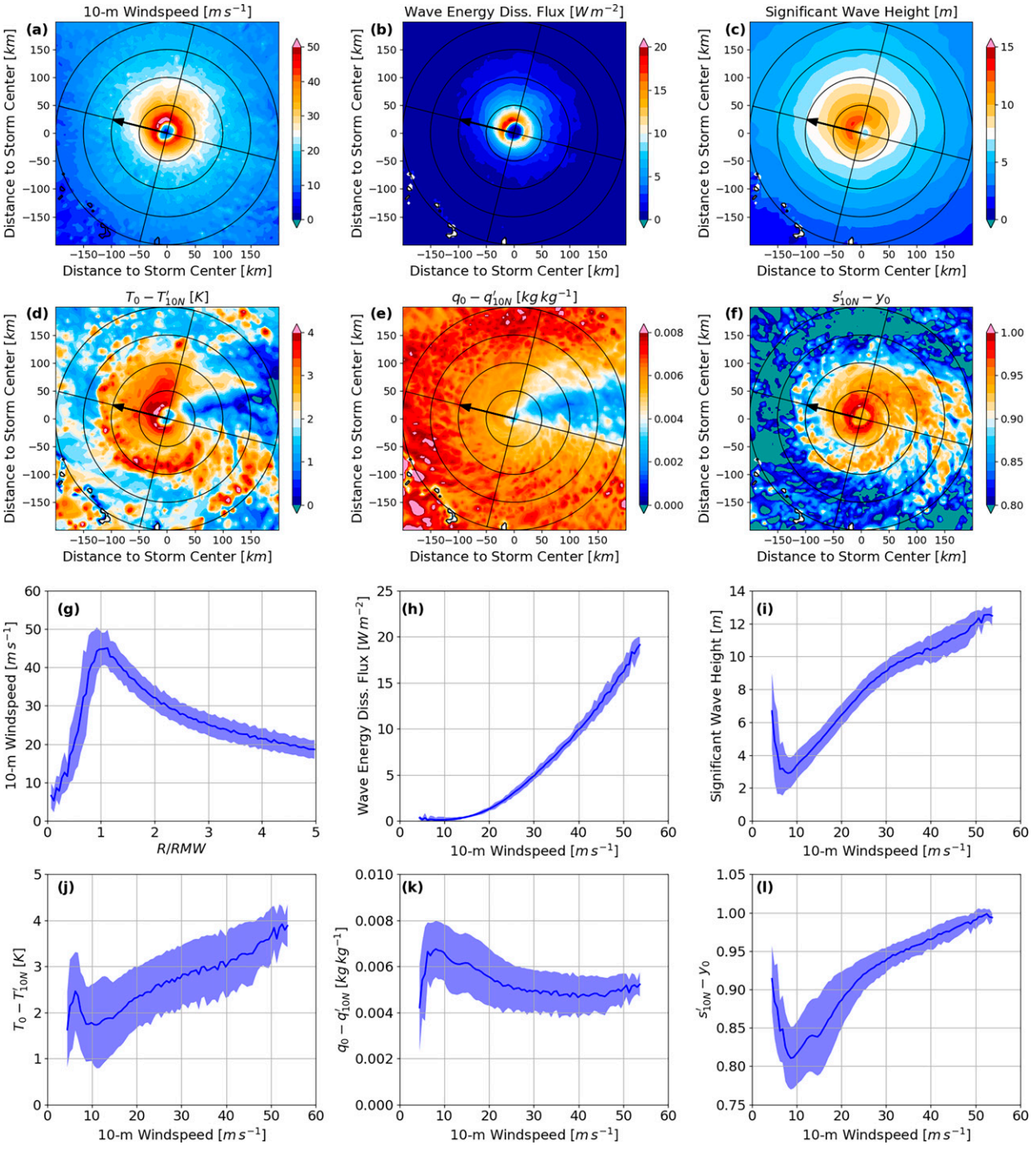


FIG. 3. Sea state and surface conditions for UWIN-CM simulation of Hurricane Dorian. (a)–(f) Maps of (a) 10-m wind speed, (b) wave energy dissipation flux, (c) significant wave height, (d) 10-m neutral, sprayless air–sea temperature difference $T_0 - T'_{10N}$, (e) 10-m neutral, sprayless air–sea specific humidity difference $q_0 - q'_{10N}$, and (f) 10-m neutral, sprayless, salt-adjusted saturation ratio $s'_{10N} - y_0$ at 0600 UTC 1 Sep 2019. (g)–(l) Mean of grid points (solid lines) with ±1 standard deviation bands (shading) for the same fields as in (a)–(f), from 0000 to 1200 UTC 1 Sep 2019.

SSGF (220 $\mu$m) is far from the peak efficiency in $E_R$, causing mean wind-based $\overline{E}_R$ (Fig. 5f) to be very low (<0.04) in all cases. Increasing $s$ causes wind-based $\overline{E}_R$ to decrease as wind speed increases. At the highest wind speeds, large droplets cause SS-based $\overline{E}_R$ to be even lower than wind-based $\overline{E}_R$, but SS-based $\overline{E}_R$ rises sharply as wind speed decreases and the SSGF favors smaller droplets. Feedback effects (discussed later) have a generally small effect on $\overline{E}_T$ and $\overline{E}_R$. We

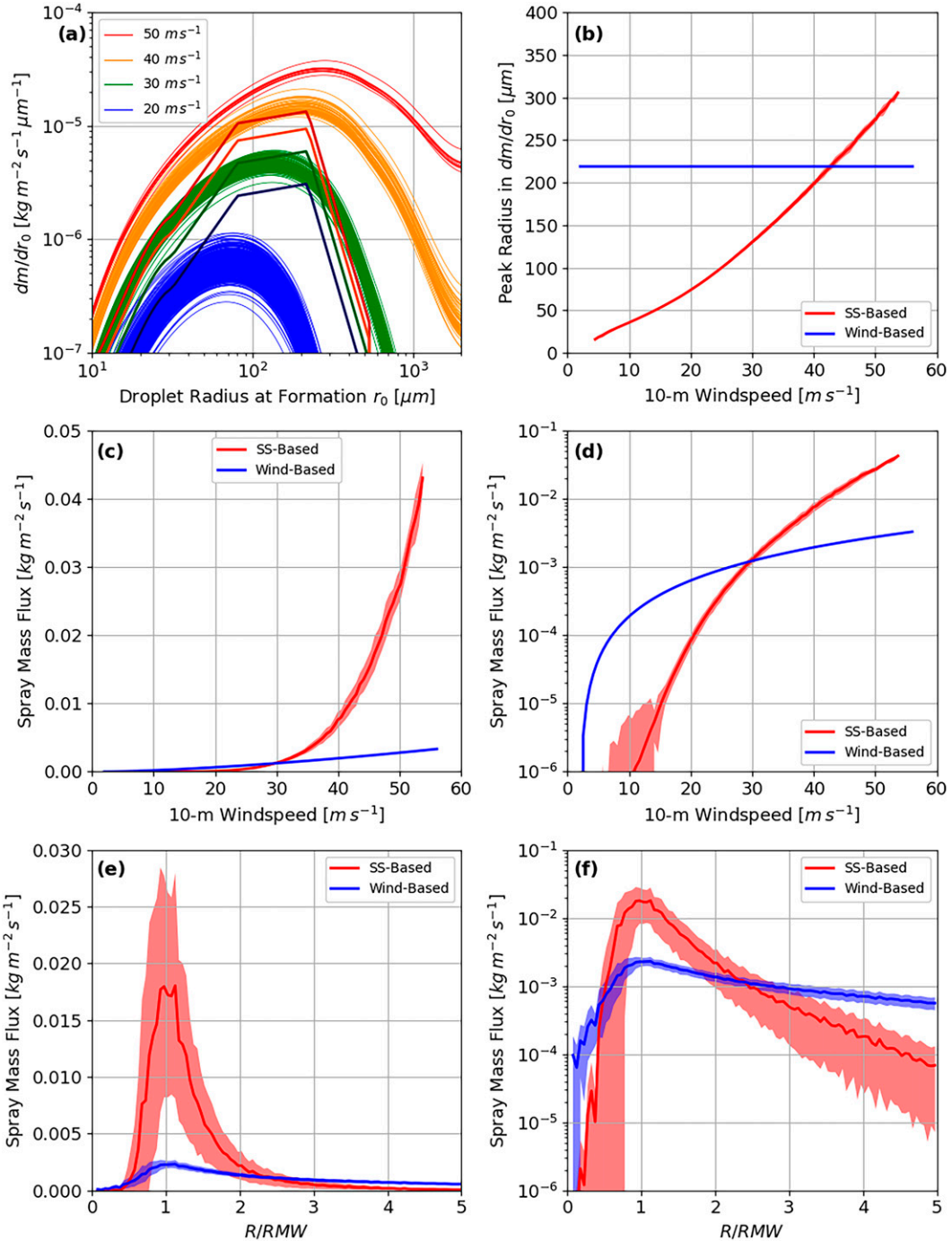


FIG. 4. Spray production for Hurricane Dorian simulation from 0000 to 1200 UTC 1 Sep 2019. Sea-state-based (SS-based) and wind-based (a) SSGFs at selected wind speeds, (b) radius of SSGF peak, and spray mass flux vs (c),(d) 10-m wind speed and (e),(f) $R$/RMW on linear and logarithmic scales. In (a), smooth curves are SS based and jointed curves are wind based. The plots in (b)–(f) show means of grid points (solid lines) with ± 1 standard deviation bands (shading).

emphasize that, in the absence of feedback, differences between wind-based and SS-based $\overline{E}_T$ and $\overline{E}_R$ are due to the shape of the SSGF alone [the influence of $M_{\rm spr}$ is removed by (13)].

We now examine the spray heat fluxes $H_{\rm SN,spr}$, $H_{L,\rm spr}$, and $H_{K,\rm spr}$. Analysis not presented shows that $H_{\rm wb,spr}$ is very small ($\lesssim$10 W m$^{-2}$ under most conditions) due to effects of low $M_{\rm spr}$ at lower wind speeds (Fig. 4c) and low $\Delta T_{\rm wb}$ at higher

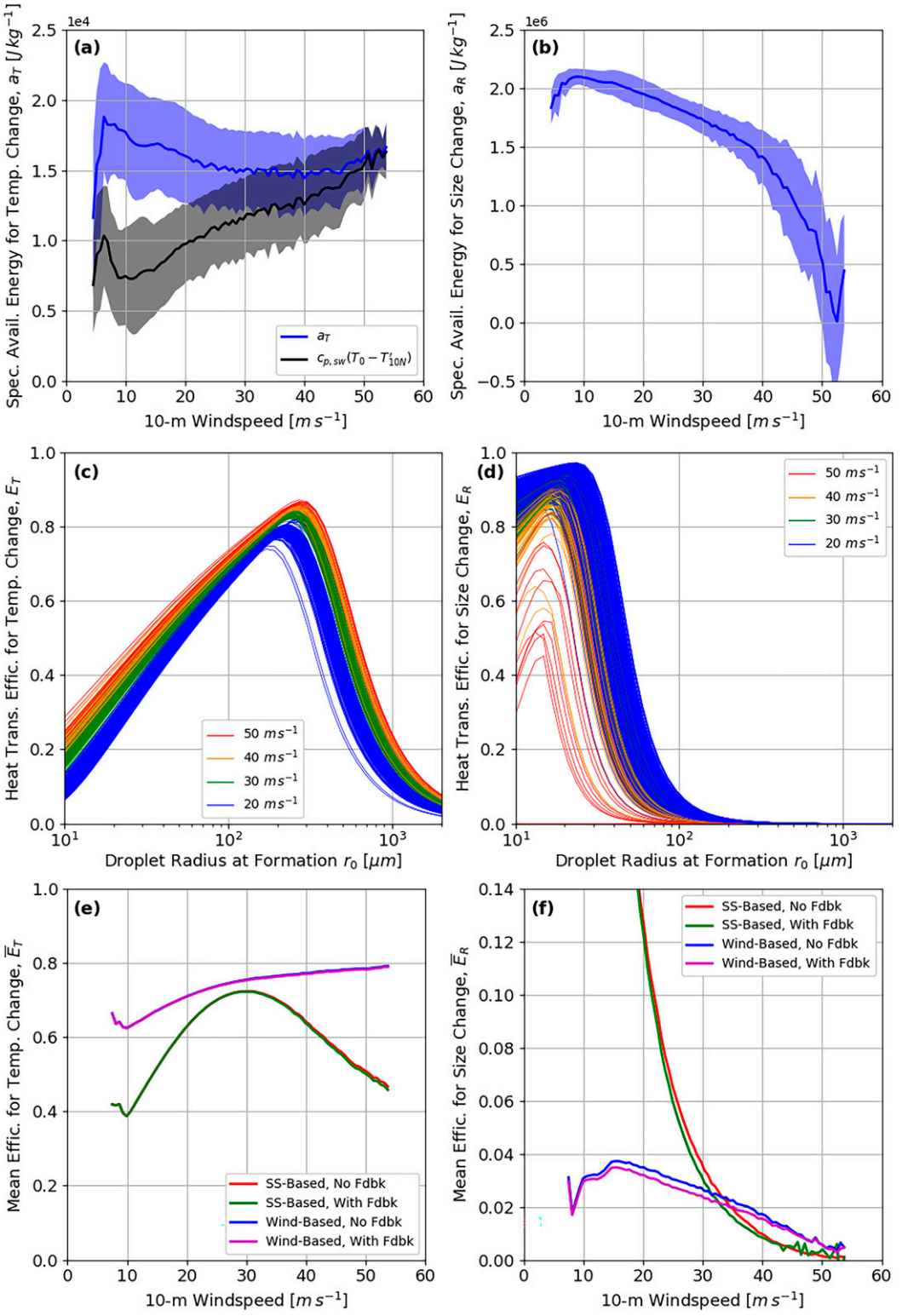


FIG. 5. Specific available energies and heat transfer efficiencies for Hurricane Dorian simulation from 0000 to 1200 UTC 1 Sep 2019. Mean (a) $a_T$ and (b) $a_R$, with $\pm 1$ standard deviation bands. For reference, the quantity $c_{p,\mathrm{sw}}(T_0 - T'_{10\mathrm{N}})$, which is $a_T$ without the wet-bulb depression contribution, is also plotted in (a). (c) $E_T$ and (d) $E_R$ without near-surface feedback at selected wind speeds. Mean (e) $\overline{E}_T$ and (f) $\overline{E}_R$, showing results with and without near-surface feedback using both SS- and wind-based SSGFs.

wind speeds (Fig. 5a). So, for the purpose of interpretation, we may consider $H_{S,\mathrm{spr}} \approx H_{T,\mathrm{spr}}$ and $H_{L,\mathrm{spr}} \approx H_{R,\mathrm{spr}}$, allowing us to interpret $H_{\mathrm{SN,spr}}$, $H_{L,\mathrm{spr}}$, and $H_{K,\mathrm{spr}}$ in terms of available energies and efficiencies.

At low wind speeds, higher $M_{\mathrm{spr}}$ and $\overline{E}_T$ for the wind-based SSGF produce larger $H_{K,\mathrm{spr}}$ (equal to $H_{T,\mathrm{spr}}$) than when using the SS-based SSGF (Fig. 6c). At higher wind speeds, very large SS-based $M_{\mathrm{spr}}$ counteracts the deficit in $\overline{E}_T$, and the SS-based SSGF produces higher $H_{K,\mathrm{spr}}$. $H_{L,\mathrm{spr}}$ (Fig. 6b) rises steadily with wind speed for both SSGFs until around 35 m s$^{-1}$, after which point it decreases due to high $s$, which attenuates both $a_R$ and $\overline{E}_R$. The shapes of $H_{L,\mathrm{spr}}$ curves depend strongly on the SSGF selected. Note that we force zero spray heat fluxes for $U_{10} < 10$ m s$^{-1}$ because this is the approximate observed threshold for producing spume droplets (e.g., Veron 2015); the wind-based SSGF produces a sharp (nonphysical) jump in $H_{L,\mathrm{spr}}$ at this threshold whereas the SS-based curves are smooth. $H_{\mathrm{SN,spr}}$ mirrors features of both $H_{K,\mathrm{spr}}$ and $H_{L,\mathrm{spr}}$ (Fig. 6a). Below approximately 45 m s$^{-1}$, $H_{R,\mathrm{spr}} > H_{S,\mathrm{spr}}$, and evaporative cooling of spray produces negative $H_{\mathrm{SN,spr}}$. For higher wind speeds, $H_{S,\mathrm{spr}} > H_{R,\mathrm{spr}}$ and $H_{\mathrm{SN,spr}}$ is positive, although it is much larger for the SS-based SSGF than for the wind-based SSGF. Replotting these results versus $R$/RMW (Figs. 6d–f), we find that the SS-based SSGF produces substantially higher (lower) $H_{K,\mathrm{spr}}$ than does the wind-based SSGF within (outside) 2 to 3RMW, with peak $H_{K,\mathrm{spr}}$ occurring at the RMW for both SSGFs. $H_{L,\mathrm{spr}}$ does not peak at the RMW but rather between 1 and 2RMW, with the SS-based SSGF producing a stronger peak that is closer to the RMW. Finally, while both SSGFs produce negative $H_{\mathrm{SN,spr}}$ outside the eyewall, the SS-based SSGF produces strong positive $H_{\mathrm{SN,spr}}$ at the RMW whereas wind-based $H_{\mathrm{SN,spr}}$ is near zero there. Feedback effects (discussed later) do not change the qualitative behavior of any spray heat fluxes.

Turning now to spray's impact on total air–sea heat fluxes (Figs. 6g–l), SS-based spray contributes strongly to the total eyewall enthalpy flux (over 12.5% mean increase at the peak), whereas the wind-based increase is much smaller (~2.5%). SS-based $H_{L,\mathrm{spr}}$ produces a mean increase of LHF over 12.5% near 1.5RMW which diminishes quickly with storm radius, whereas wind-based $H_{L,\mathrm{spr}}$ produces a mean increase of nearly 10% between 2 and 5RMW. Both SSGFs reduce the SHF strongly outside the eyewall. Mean increase in SHF at the RMW is over 20% using the SS-based SSGF but is near zero for the wind-based SSGF.

With spray heat fluxes described, we now characterize their feedback effects on the near-surface layer. Spray-layer warming/cooling (Fig. 7a) mirrors $H_{\mathrm{SN,spr}}$ (Fig. 6d), with cooling outside the eyewall for both SSGFs and warming at the RMW for the SS-based SSGF. Spray-layer moistening (Fig. 7c) mirrors $H_{L,\mathrm{spr}}$ (Fig. 6e). Heating/cooling and moistening cause $s$ to increase under all conditions for both SSGFs, except at the RMW using the SS-based SSGF, where $s$ decreases due to the stronger impact of warming than of moistening (Fig. 7e).

Cooling of the spray layer amplifies $H_{S,\mathrm{spr}}$ for all conditions for both SSGFs, resulting in $\alpha_S > 1.0$, except at the RMW using the SS-based SSGF, where warming produces $\alpha_S < 1.0$ (Fig. 7b). Outside the eyewall, increased $s$ reduces $H_{L,\mathrm{spr}}$, causing $\beta_L < 1.0$ (Fig. 7d). At the RMW, decreased $s$ for the SS-based SSGF increases $H_{L,\mathrm{spr}}$, causing $\beta_L > 1.0$ (note that $\beta_L$ can be very large when $H'_{L,\mathrm{spr}}$ is near zero). Because $H_{L,\mathrm{spr}} \approx H_{R,\mathrm{spr}}$, $\beta_L \approx \beta_S$ ($\beta_S$ is thus not shown). $\gamma_S$ and $\gamma_L$ do not depend on the SSGF but rather on the thickness of the spray layer. Both peak above 0.9 at the RMW where waves are highest and decrease with distance outward, remaining high (~0.85) at 5RMW (Fig. 7f).

Overall, the impacts of feedback on spray heat fluxes are modest (feedback coefficients are generally close to 1.0), as reflected in the efficiencies (Figs. 5e,f) and heat fluxes (Figs. 6a–f). The feedback modification to the interfacial fluxes is also small, as seen by comparing interfacial fluxes without spray (black lines) and with SS-based spray feedback (gray lines) in Figs. 6g–i. The modest impact of near-surface feedback on surface-layer thermodynamic variables and heat fluxes can be understood as follows. By injecting heat and moisture into the spray layer away from the surface, spray bypasses the region of highest resistance to vertical turbulent transfer (i.e., the lowest eddy diffusivity). Away from the surface, only a small increase in the vertical gradients of $\theta$ and $q$ is required to drive the additional spray heat fluxes upward, so the surface layer can accommodate the increase in total heat fluxes due to spray without large changes to the vertical thermodynamic profiles. We should also point out that the SS-based and wind-based SSGFs produce unique feedback behavior. For instance, the SS-based (wind-based) model produces large positive (near-zero) $H_{\mathrm{SN,spr}}$ at the RMW (Fig. 6d), which causes large (near-zero) spray-layer warming (Fig. 7a) and a decrease (almost no change) in spray-layer $s$ (Fig. 7e) at the RMW. Consequently, $H_{L,\mathrm{spr}}$ at the RMW (Fig. 6e) is amplified by feedback for the SS-based model but is essentially unchanged for the wind-based model.

Finally, we examine spray's impact on heat transfer coefficients (with near-surface feedback included). Both SSGFs substantially decrease $C_{h,10\mathrm{N}}$ for $U_{10\mathrm{N}} \lesssim 45$ m s$^{-1}$, and the SS-based SSGF increases $C_{h,10\mathrm{N}}$ considerably above 45 m s$^{-1}$ (Fig. 8a). Both SSGFs increase $C_{q,10\mathrm{N}}$, but the SS-based model produces a stronger effect at higher wind speeds (Fig. 8b). Wind-based spray has almost no effect on $C_{k,10\mathrm{N}}$, but SS-based spray produces $C_{k,10\mathrm{N}}$ that levels off and then increases for $U_{10\mathrm{N}} \gtrsim 30$ m s$^{-1}$ (Fig. 8c).

### d. *Air–sea heat fluxes with spray in diverse and complex TC conditions*

We now expand upon the previous sections' findings by examining sea-state-dependent air–sea heat fluxes with spray across a diverse set of TC simulations covering a wide range of environments. Spray calculations in this section are made using the SS-based SSGF only, and near-surface feedback is always included. In addition to Dorian, we examine (Fig. 9) Hurricanes Harvey (2017), Michael (2018), and Florence (2018) and Typhoon Fanapi (2010). For each new storm, open ocean and coastal periods were selected. Twelve-hour open-ocean periods (Mic-O, Flo-O, Fan-O, Har-O) were selected when the storms were translating in the open ocean with little curvature, ensuring that the wave fields are not disrupted by

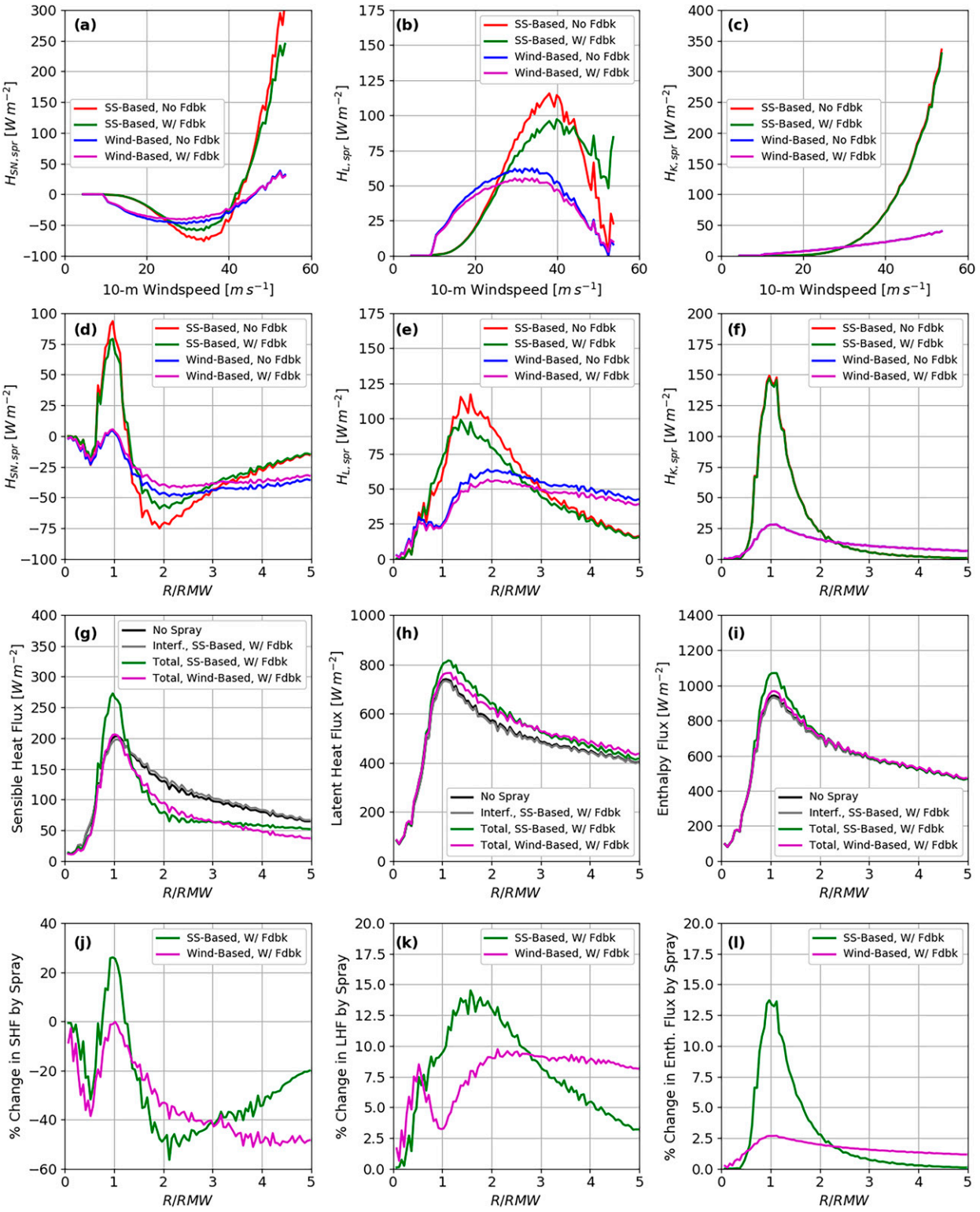


FIG. 6. Spray and total heat fluxes for Hurricane Dorian simulation from 0000 to 1200 UTC 1 Sep 2019. Mean spray (a),(d) net sensible heat, (b),(e) latent heat, and (c),(f) enthalpy fluxes vs (a)–(c) 10-m wind speed and (d)–(f) *R*/RMW. Mean interfacial and total (g) sensible heat, (h) latent heat, and (i) enthalpy fluxes vs *R*/RMW. Mean percentage change in (j) sensible heat, (k) latent heat, and (l) enthalpy fluxes due to spray vs *R*/RMW.

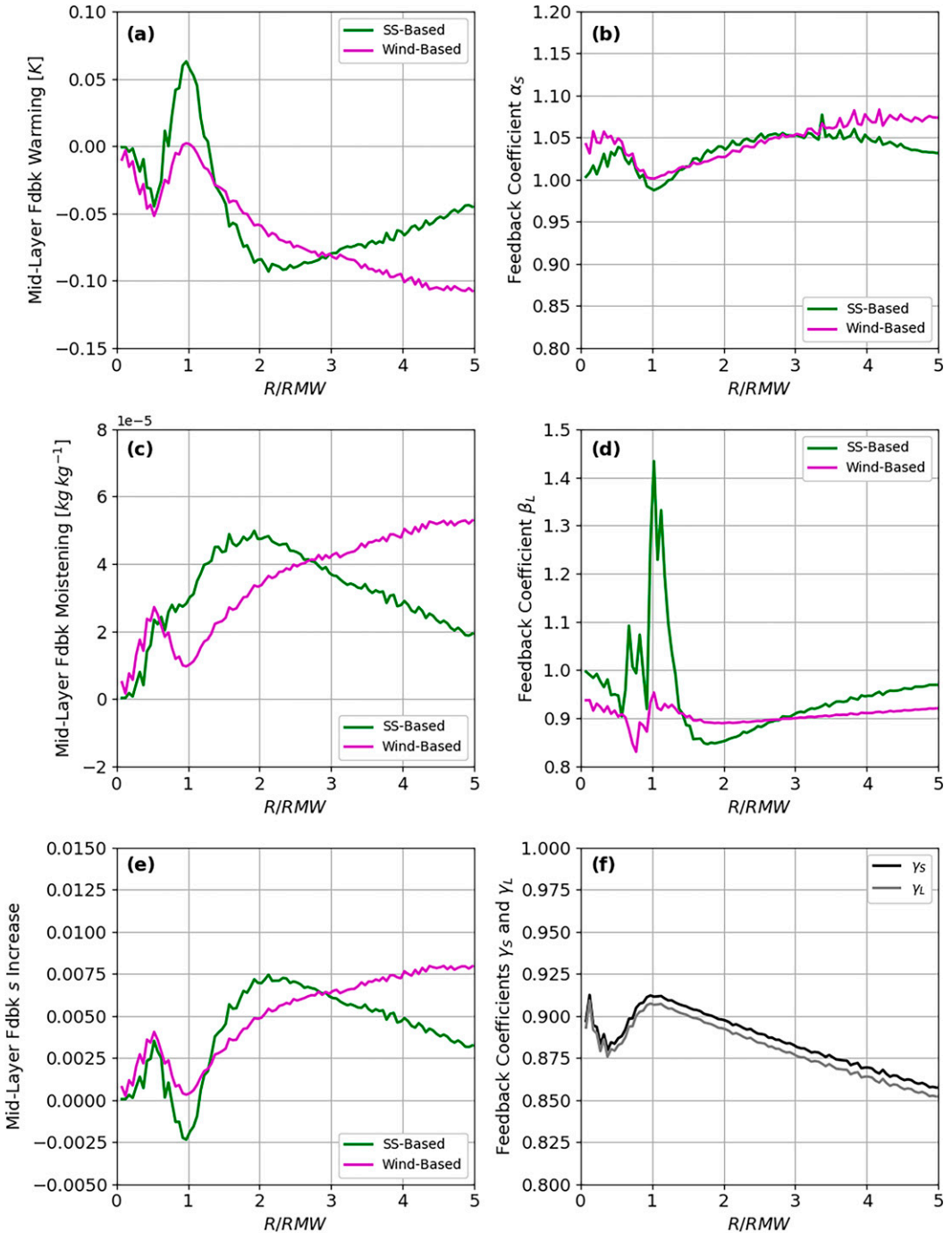


FIG. 7. Feedback modifications to thermodynamic variables at the middle of the spray layer ($\delta/2$) and feedback coefficients for Hurricane Dorian simulation from 0000 to 1200 UTC 1 Sep 2019. Mean mid-spray-layer changes to (a) air temperature, (c) specific humidity, and (e) saturation ratio. Mean feedback coefficients (b) $\alpha_S$, (d) $\beta_L$, and (f) $\gamma_S$ and $\gamma_L$.

changing storm direction. Coastal periods were defined to demonstrate the influence of seafloor interaction (i.e., wave shoaling) on heat fluxes. For storms making landfall over continental shelves, we select coastal periods (Mic-C, Flo-C, Har-C) where the product of dominant wavenumber and water depth averaged within 1RMW is less than $\pi$ (this parallels the classical linear deep-water wave definition; e.g., Young 1999). For Fanapi, which is over deep water until landfall, we select a 9-h period preceding landfall (Fan-C) for comparison.

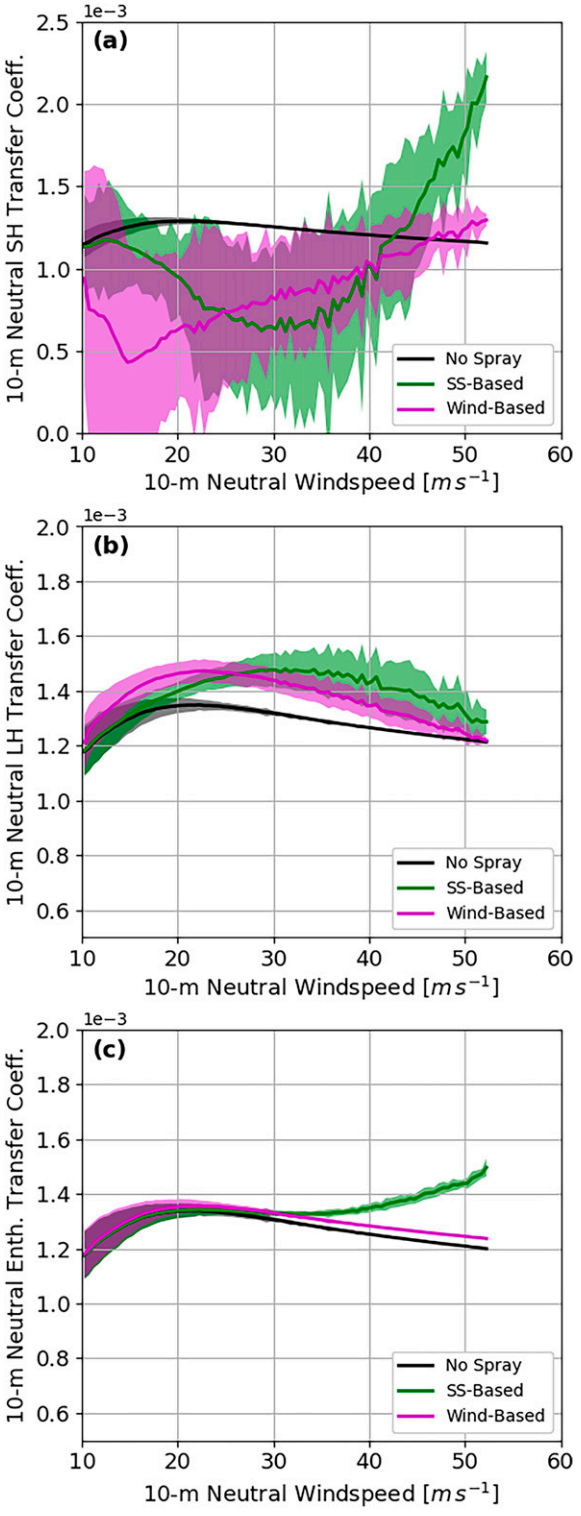


FIG. 8. The 10-m neutral heat transfer coefficients for Hurricane Dorian simulation from 0000 to 1200 UTC 1 Sep 2019. Mean values (solid lines) with ±1 standard deviation bands (shading) for heat transfer coefficients for (a) sensible heat, (b) latent heat, and (c) enthalpy, showing results without spray and with SS-based and wind-based SSGFs. All spray results include near-surface feedback.

Per (1), the spray mass flux is modulated by wave properties including $\varepsilon$ (holding other properties constant, $M_{\text{spr}}$ increases as TKE due to $\varepsilon$ increases), $H_s$ (the breaking penetration depth increases with $H_S$; holding other properties constant, $M_{\text{spr}}$ decreases as increasing $H_s$ spreads dissipation vertically), and $C_{p,d}$ (holding other properties constant, increasing $C_{p,d}$ reduces $M_{\text{spr}}$ by decreasing the wave-relative ejection velocity of droplets). Comparison of these properties and $M_{\text{spr}}$ across storms (Fig. 10) shows how storm-scale wave behavior controls $M_{\text{spr}}$. Open ocean storms and Fan-C, which do not experience shoaling, have dissipation curves that group together, relatively high $H_S$, and high $C_{p,d}$. Shoaling (Mic-C, Flo-C, Har-C) causes a strong increase in dissipation (due to increased breaking), a reduction in $H_s$ (by removing energy from the spectrum), and a reduction in $C_{p,d}$. These differences in behavior create two groups of curves for $M_{\text{spr}}$ (i.e., shoaling and nonshoaling), with shoaling cases experiencing higher $M_{\text{spr}}$ than nonshoaling cases for the same wind speed. Note that even within nonshoaling cases, the influence of storm-specific differences in sea state can be seen, as nonshoaling $M_{\text{spr}}$ curves are reordered relative to dissipation curves due to $H_s$ and $C_{p,d}$. Note also that curves for Dor-O from sections 4a–4c are reproduced identically in Fig. 10 and future figures.

Behavior of $a_T$ (Fig. 11a) is storm specific, with mean values ranging between roughly $1 \times 10^4$ and $2 \times 10^4$ J kg$^{-1}$. Analysis not presented shows that at high winds most of the variation in $a_T$ among cases arises from variation in the air–sea temperature difference rather than the wet-bulb depression. $a_R$ (Fig. 11b) varies according to storm-scale behavior of $s'_{10N} - y_0$ (Fig. 11c). Although all cases experience a drop in $a_R$ with increasing wind speed, the magnitude of $a_R$ at the highest wind speeds is very sensitive to the corresponding value of $s'_{10N} - y_0$, with $a_R$ varying between approximately $1.5 \times 10^6$ and 0 J kg$^{-1}$ as $s'_{10N} - y_0$ varies between 0.95 and 1.0. The relationship between $s'_{10N} - y_0$ and $q_0 - q'_{10N}$ is storm specific (Fig. 11d), indicating that spray LHF cannot be scaled using the traditional turbulent thermodynamic scale $q_0 - q'_{10N}$.

For all storm periods, $\overline{E}_T$ follows the inverted U-shape caused by the SS-based SSGF's transition from smaller to larger droplets as wind-wave processes intensify (Fig. 11e). $\overline{E}_T$ shows variation among cases due to the impact of $H_s$ on $\tau_f$ (cf. to Fig. 10b), with larger waves increasing efficiency by lengthening droplet residence times. $\overline{E}_R$ is high at low wind speeds and plummets to near zero as wind speed increases, with case-to-case variation arising from storm-scale differences in $H_s$ and $s'_{10N} - y_0$. (Fig. 11f).

We now address spray heat fluxes across our diverse set of storm cases and their impacts on total heat fluxes. Variation in $H_{K,\text{spr}}$ (Fig. 12c) arises from shoaling impacts on $M_{\text{spr}}$ (Fig. 10d), case-specific variation in $a_T$ (Fig. 11a), and modulation of $\overline{E}_T$ by $H_s$ (Fig. 11e). Shoaling cases produce consistently higher $H_{K,\text{spr}}$ than nonshoaling cases. Shoaling impacts on $M_{\text{spr}}$ and control of both $a_R$ and $\overline{E}_R$ by $s'_{10N} - y_0$ (Figs. 11b,c,f) dominate variation in $H_{L,\text{spr}}$ (Fig. 12b). High-$s$ cases (e.g., Dor-O, Mic-O) produce $H_{L,\text{spr}}$ that remains low or even declines at the highest wind speeds, whereas low-$s$ cases (e.g., Mic-C, Fan-C) produce $H_{L,\text{spr}}$ that rises continuously with wind speed. All aforementioned

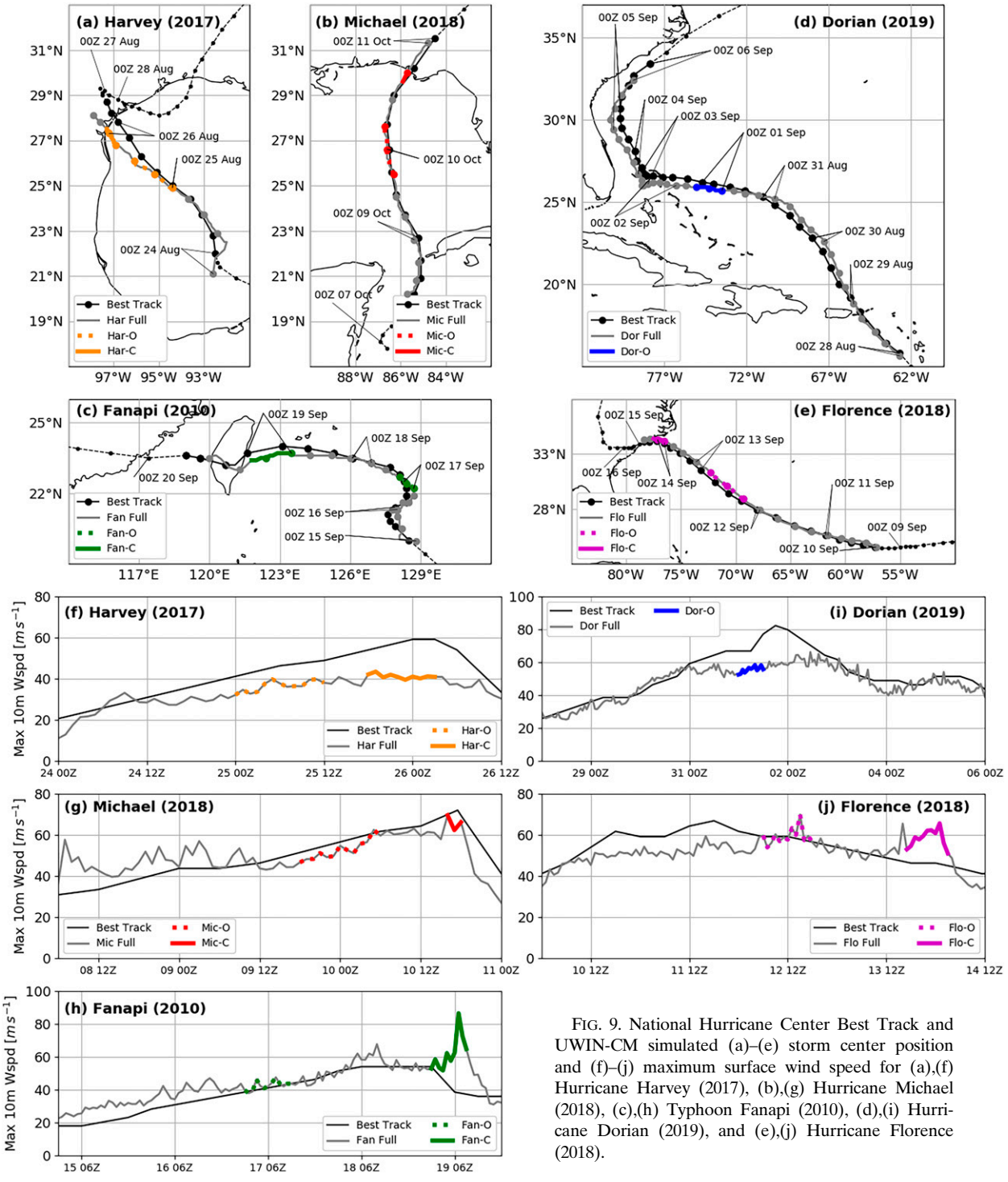


FIG. 9. National Hurricane Center Best Track and UWIN-CM simulated (a)–(e) storm center position and (f)–(j) maximum surface wind speed for (a),(f) Hurricane Harvey (2017), (b),(g) Hurricane Michael (2018), (c),(h) Typhoon Fanapi (2010), (d),(i) Hurricane Dorian (2019), and (e),(j) Hurricane Florence (2018).

influences apply also to $H_{SN,spr}$ and produce a wide range of behavior (Fig. 12a). When $H_{K,spr}$ is low and/or $H_{L,spr}$ is high (e.g., Fan-C, Flo-O), $H_{SN,spr}$ is near zero or negative at all but the highest wind speeds. When $H_{K,spr}$ is high and/or $H_{L,spr}$ is low (e.g., Dor-O), $H_{SN,spr}$ becomes very large at high wind speeds. In all cases, negative $H_{SN,spr}$ occurs between $U_{10}$ of approximately 20 and 40 m $s^{-1}$. In $R$/RMW coordinates (Figs. 12d–f), peak $H_{K,spr}$ occurs near the RMW, but peak $H_{L,spr}$ occurs between 1 and 1.5RMW. Some cases (i.e., Dor-O, Mic-C, Flo-C) have strong positive mean $H_{SN,spr}$ in the eyewall, but all other cases show negative $H_{SN,spr}$ there. All cases show negative $H_{SN,spr}$ beyond 1.5RMW.

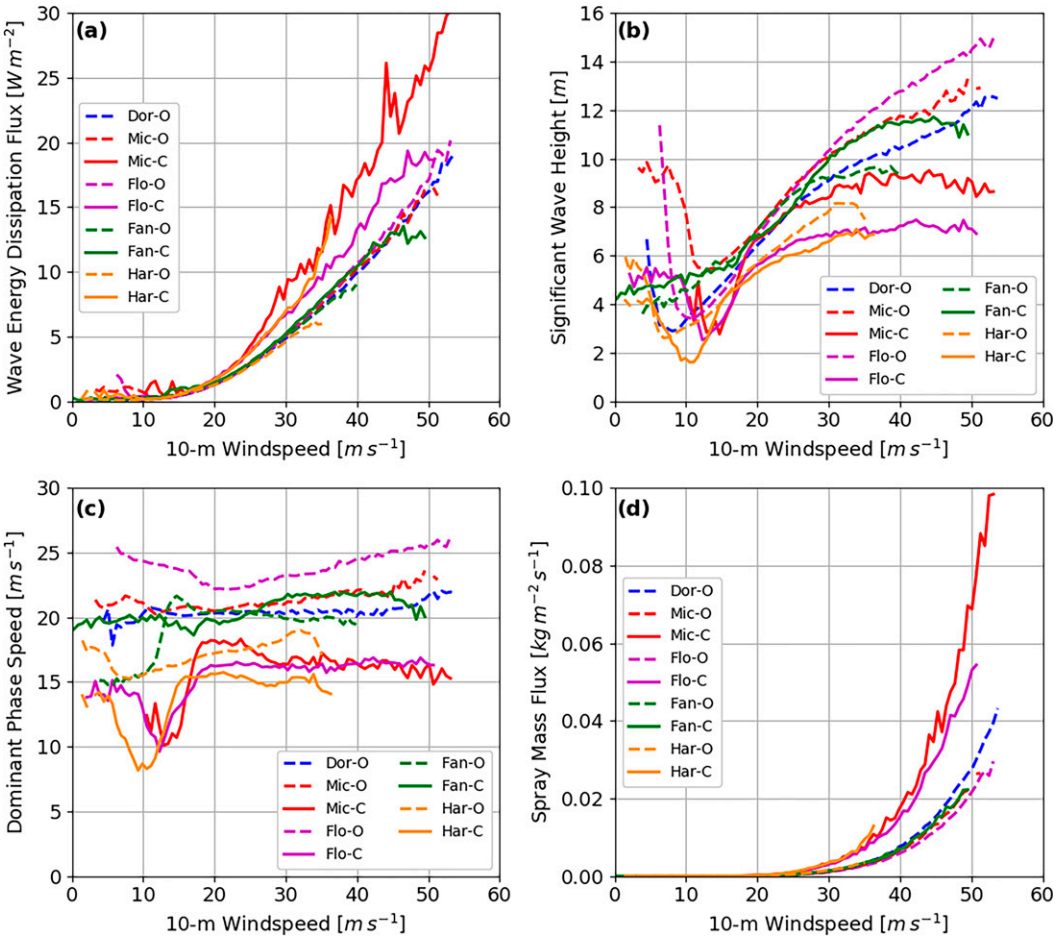


FIG. 10. Mean (a) wave dissipation flux, (b) significant wave height, (c) dominant phase speed, and (d) spray mass flux vs 10-m wind speed across selected periods of UWIN-CM simulations of five storms.

Spray augments the turbulent heat fluxes (Figs. 12g–i) to different degrees (Figs. 12j–l) depending on storm-specific wave and thermodynamic characteristics. Strong shoaling cases (Mic-C, Flo-C) have the strongest spray contribution to enthalpy fluxes (35% mean increase in enthalpy flux at the RMW for Mic-C). Spray increases enthalpy fluxes most strongly at the RMW for all cases, with percentage increase declining smoothly at larger radii. Because spray and turbulent LHFs depend on different thermodynamic properties, spray augmentation of the turbulent LHF depends on the storm-specific relationship between $s'_{10N} - y_0$ and $q_0 - q'_{10N}$. In all but the weakest case (Har-O), the largest mean increase of LHF due to spray is over 10%. Spray contribution to total SHF varies widely due to storm-scale differences in wave properties and evaporative cooling rates. Spray may produce a mean change in SHF at the RMW above 30% (Mic-C; due to high $H_{K,\mathrm{spr}}$) or below −60% (Fan-C; due to high $H_{L,\mathrm{spr}}$). Depending on the magnitude of $H_{L,\mathrm{spr}}$, spray may produce a mean reduction of SHF at large radii of below 20% (Har-O) or nearly 100% (Mic-C).

Spray impacts on heat transfer coefficients are shown in Fig. 13. Heat transfer coefficients without spray collapse for all cases, but there is substantial spread in all three coefficients across the selected cases when spray is included. In extreme cases (Mic-C, Fan-C), spray evaporative cooling is so strong that it completely negates the turbulent SHF, producing $C_{h,10N}$ below zero. In all cases, $C_{k,10N}$ levels off and then rises for $U_{10N} \gtrsim 40\,\mathrm{m\,s^{-1}}$ when spray is included.

Finally, we summarize the behavior of heat fluxes with spray by tracking several metrics for spray through the full simulation time period for all storms. Spray mass flux at the RMW for all storms falls near a common curve when plotted versus peak azimuthal-mean 10-m wind speed, with notable deviation from this curve occurring for shoaling cases (Fig. 14a). Percent increase in enthalpy flux at the RMW shows a very similar pattern, reflecting the strong connection between spray mass and enthalpy fluxes (Fig. 14f). Mean percent increase in LHF outside the RMW due to spray increases with peak azimuthal-mean wind speed, but there is a large spread in results due to storm-specific patterns in waves and thermodynamics outside the eyewall (Fig. 14e). Due to the coupling of sensible and latent spray heat fluxes by evaporative cooling, mean percent change in SHF outside the RMW due to spray shows a similar but negative pattern to that for LHF, with larger magnitudes of change

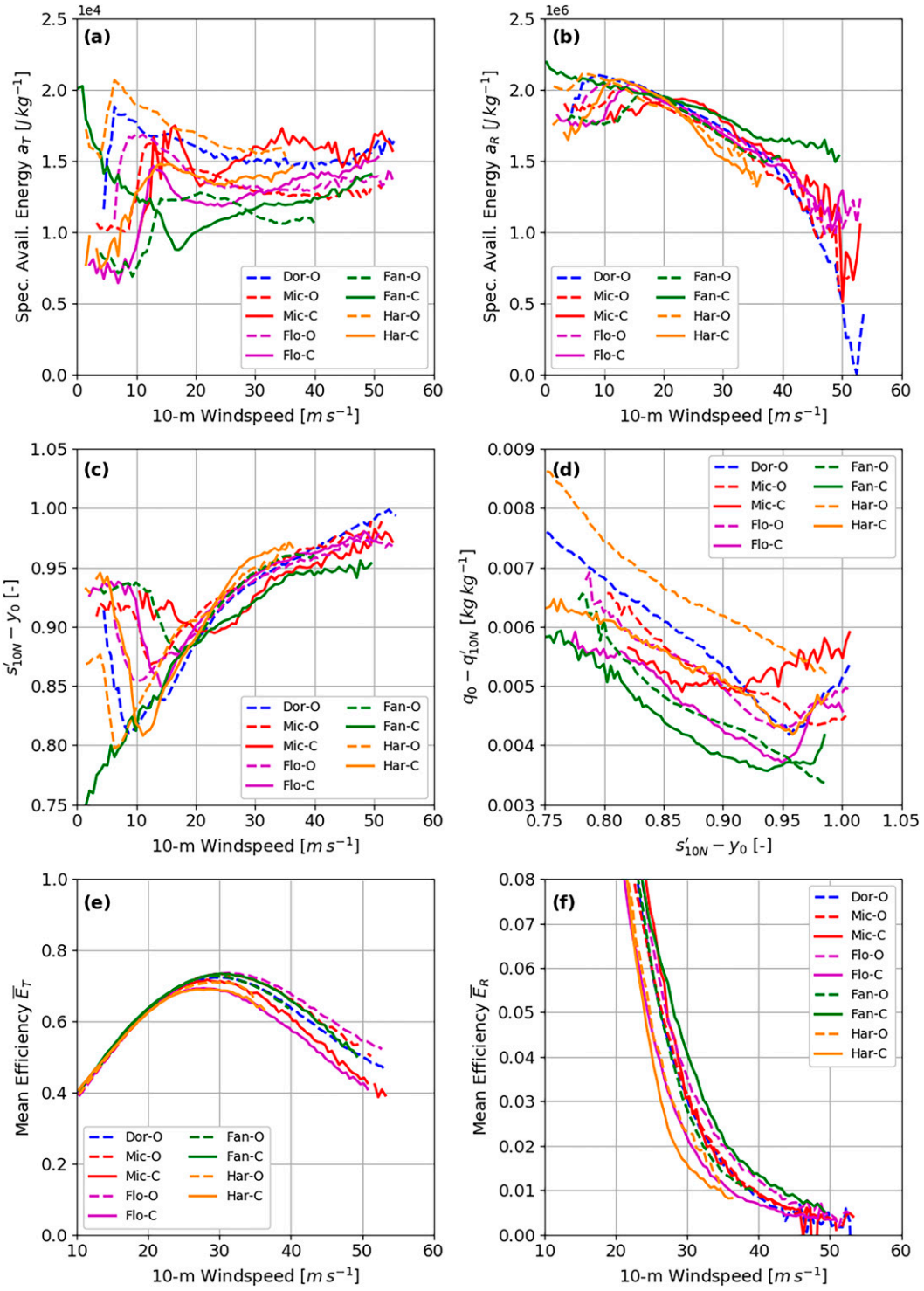


FIG. 11. Mean (a) $a_T$, (b) $a_R$, (c) 10-m neutral, sprayless, salt-adjusted saturation ratio $s'_{10N} - y_0$, (e) efficiency $\overline{E}_T$, and (f) efficiency $\overline{E}_R$ vs 10-m wind speed across selected periods of UWIN-CM simulations of five storms. (d) 10-m neutral, sprayless air–sea specific humidity difference $q_0 - q'_{10N}$ vs $s'_{10N} - y_0$ for the same periods.

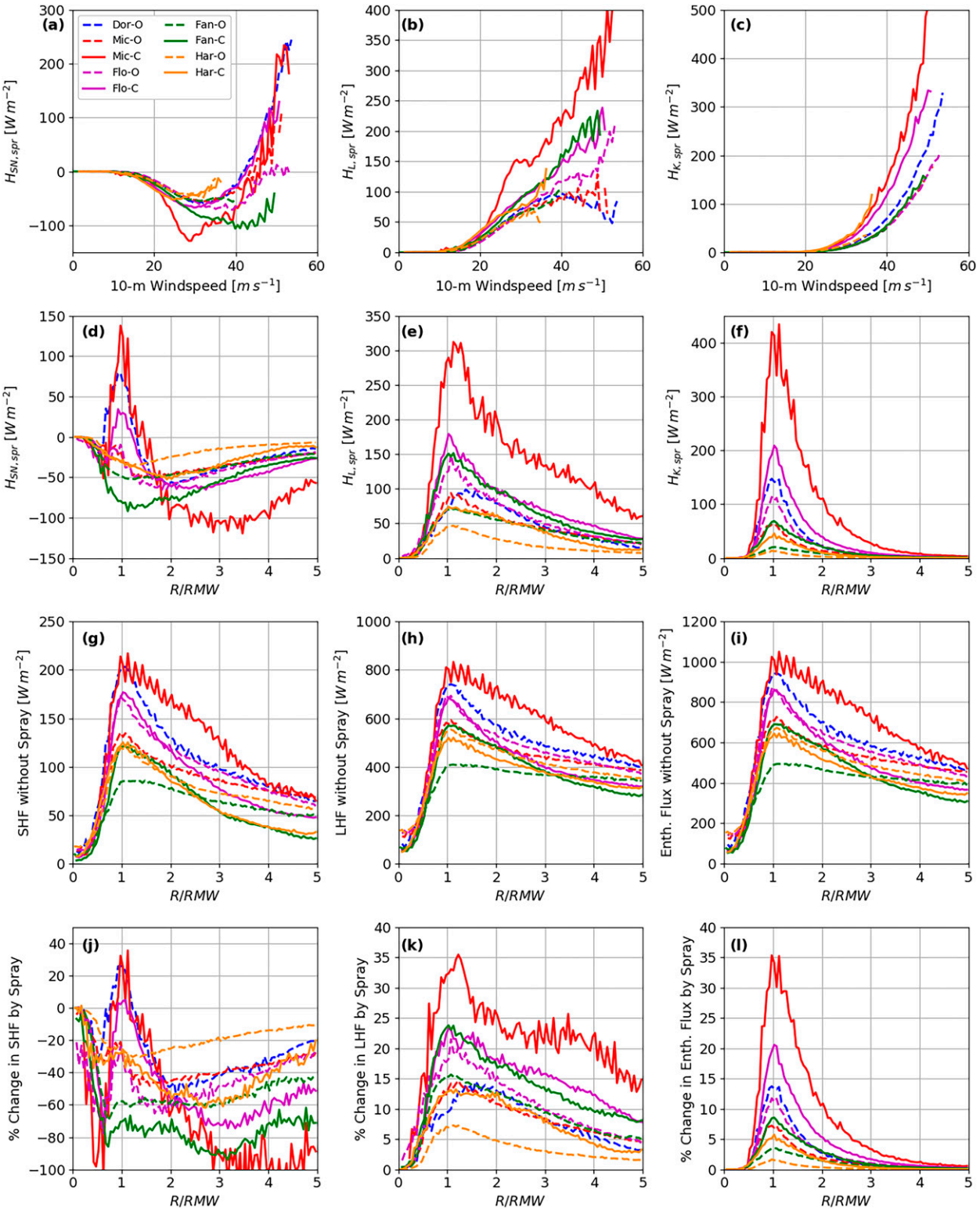


FIG. 12. Spray and total heat fluxes across selected periods of UWIN-CM simulations of five storms. Mean spray (a),(d) net sensible heat, (b),(e) latent heat, and (c),(f) enthalpy fluxes vs (a)–(c) 10-m wind speed and (d)–(f) *R*/RMW. Mean (g) sensible heat, (h) latent heat, and (i) enthalpy fluxes without spray vs *R*/RMW. Mean percent change in (j) sensible heat, (k) latent heat, and (l) enthalpy fluxes due to spray vs *R*/RMW.

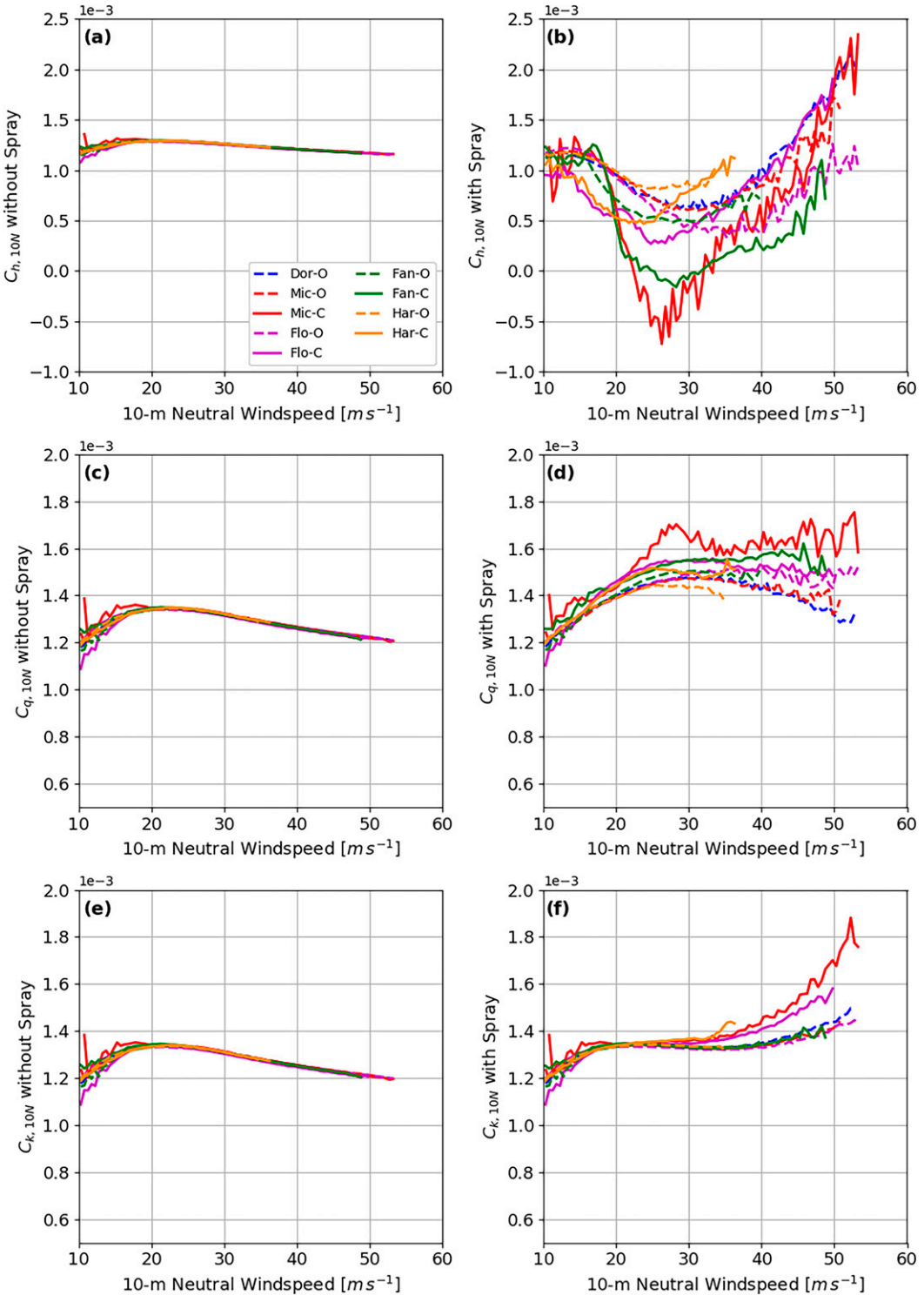


FIG. 13. Mean heat transfer coefficients for selected periods of UWIN-CM simulations of five storms. (a),(b) $C_{h,10N}$, (c),(d) $C_{q,10N}$, and (e),(f) $C_{k,10N}$, showing results (a),(c),(e) without spray and (b),(d),(f) with spray.

due to turbulent LHF being generally much larger than turbulent SHF (Fig. 14d). Spray mean change to SHF at the RMW (Fig. 14c) is generally negative below 35 m $s^{-1}$ but may become either strongly negative or strongly positive at higher wind speeds. The tendency for eyewall SHF change to be positive or negative seems to correspond to the eyewall saturation ratio (Fig. 14b), with high-*s* cases (e.g., Dor-O) increasing SHF and low-*s* cases (e.g., Fan-C) reducing SHF. Shoaling cases (e.g.,

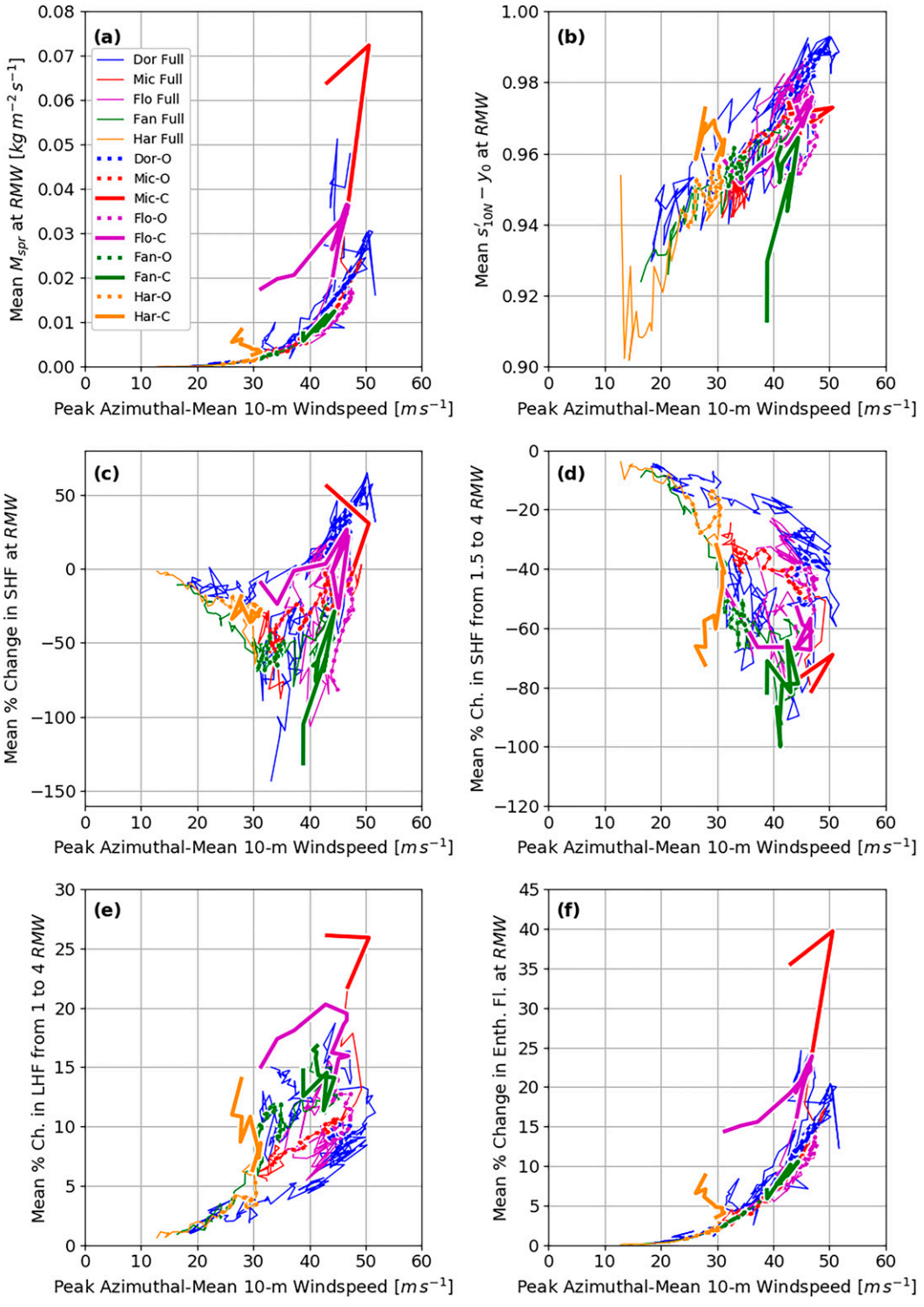


FIG. 14. Time traces of metrics for spray through the full simulation time period for all storms (calculations performed hourly). (a) Mean $M_{\text{spr}}$ at the RMW, (b) mean $s'_{10\text{N}} - y_0$ at the RMW, (c) mean percentage change in SHF due to spray at the RMW, (d) mean percentage change in SHF due to spray between 1.5 and 4RMW, (e) mean percentage change in LHF due to spray between 1 and 4RMW, and (f) mean percentage change in enthalpy flux due to spray at the RMW. All metrics are plotted vs the peak azimuthal-mean 10-m wind speed.

Mic-C, Flo-C) seem to have increasing SHF despite relatively low $s'_{10N} - y_0$ due to shoaling-enhanced $H_{K,spr}$.

Because this study has demonstrated that spray effects may be storm specific, it is reasonable to wonder if they can be predicted by storm characteristics such as size and speed. While a full assessment is beyond the scope of this work, we briefly address this idea in Fig. 15 by tracking several metrics for spray against storm size (which indicates the areal extent of the high-wind regime where spray is most active) and storm translation speed (which affects the asymmetry of the wind and wave fields that drive spray). Spray impact on eyewall enthalpy flux does not show a clear dependence on storm size [measured as the radius of 17 m $s^{-1}$ (gale force) winds] (Fig. 15e). Spray impact on LHF outside the RMW generally increases with storm size (Fig. 15c). Spray tends to increase eyewall SHF for smaller storms and decrease it for larger storms (Fig. 15a). There is no clear dependence of any of the preceding three metrics on storm translation speed (Figs. 15b,d,f).

## 5. Conclusions

In this study, we present a new sea-state-dependent air–sea heat flux parameterization with spray and apply it over a wide range of winds, waves, and atmospheric and oceanic conditions using UWIN-CM output from five fully coupled atmosphere–wave–ocean TC simulations. Our spray parameterization models the physical processes of wave-dependent spray generation, transport, heat transfer, and near-surface feedback, allowing physical connections between waves, thermodynamics, spray, and heat fluxes to be explored. Testing our parameterization using UWIN-CM provides access to physically consistent sets of surface conditions that cover a wide range of TC environments. We believe that this study represents the first time that a sea-state-based SSGF with variable shape has been exercised and examined broadly across a range of simulated TC environments to characterize spray's impact on heat fluxes. It thus represents a valuable benchmark for understanding sea-state-based spray effects that may inform future work incorporating these processes into models.

Our sea-state-based SSGF produces droplet size distributions that favor larger droplets as wind speed increases, reflecting findings from a recent laboratory study (OS16). Sea-state-based spray mass flux differs substantially from traditional wind-based predictions. Sea-state-based spray mass flux is approximately one order of magnitude higher (lower) than traditional wind-based mass flux at $U_{10}$ = 50 (20) m $s^{-1}$ and is modulated by wave properties such as wave dissipation, significant wave height, and dominant phase speed, which may be uncorrelated to $U_{10}$. Wave shoaling in shallow water greatly increases sea-state-based spray mass flux by increasing dissipation and decreasing wave height and phase speed.

Spray heat fluxes are controlled by the total mass of spray generated, the energy available for heat transfer within that spray, and the efficiency with which the near-surface flow extracts that energy from the droplet sizes present. High eyewall $s$ is ubiquitous in TCs and severely reduces both the energy available and the efficiency of transfer for heat transfer due to size change. Heat transfers due to temperature and size change are most efficient in high winds for droplets with $r_0$ near 300 and 20 $\mu$m, respectively, and they are extremely attenuated for droplets with $r_0$ above 1000 and 100 $\mu$m, respectively. Because wind-based and sea-state-based SSGFs possess different proportions of droplet sizes, they can produce population-averaged heat transfer efficiencies that differ substantially. The wave field modulates heat transfer efficiency by controlling the ejection height, and therefore residence time, of droplets.

Sea-state-based spray enthalpy flux peaks at the RMW. Spray LHFs may be severely attenuated in the eyewall due to high $s$, confirming the strong control of spray effects by $s$ found by Shpund et al. (2012), but spray LHFs consistently produce a moistening and cooling effect outside the eyewall. Net sea-state-based spray SHF can be either positive or negative at the RMW depending on the relative strengths of spray enthalpy and latent heat fluxes.

Sea-state-based spray produces a mean increase in enthalpy flux at the RMW over 35% for Hurricane Michael at landfall, which experiences strong shoaling effects, and generally produces mean increases of 5%–20% when peak azimuthal-mean 10-m wind speed is between 40 and 50 m $s^{-1}$. Mean increase in LHF between 1 and 4RMW is generally 5%–20% for peak azimuthal-mean wind speed between 30 and 50 m $s^{-1}$, with wide variation due to waves and surface thermodynamics. Spray decreases the SHF outside the eyewall in all tested scenarios, but spray may increase or decrease SHF at the RMW. Spray increase (decrease) of eyewall SHF corresponds to high (low) eyewall $s$ and tends to occur in smaller (larger) storms. SHF decrease outside the eyewall could potentially increase boundary layer stability and enhance inflow to the inner core (Lee and Chen 2014), and changes of stability in the eyewall due to spray SHF could impact convection.

Traditional heat transfer coefficient scaling fails when spray is present because spray introduces physical interactions (at least 6) that cannot be characterized by traditional wind and thermodynamic variables (i.e., $U_{10}$, $T_0 - T'_{10N}$, and $q_0 - q'_{10N}$). These interactions are 1) spray generation depends strongly on sea state, which may be uncorrelated to wind, especially in coastal regions, 2) droplet heat transfer efficiency depends on the droplet ejection height, which is governed by sea state, 3) the wet-bulb depression, in addition to $T_0 - T'_{10N}$, governs $H_{T,spr}$, 4) $H_{R,spr}$ depends on $s'_{10N} - y_0$ rather than $q_0 - q'_{10N}$, 5) droplet sensible and latent heat fluxes are coupled through evaporative cooling, and 6) all droplet heat fluxes are coupled through near-surface feedback. Interactions 1, 2, 4, 5, and 6 apply to $C_{h,10N}$. Interactions 1, 2, 3, 4, and 6 apply to $C_{q,10N}$. Interactions 1, 2, 3, and 6 apply to $C_{k,10N}$. Although results are case-dependent, our sea-state-based spray model consistently produces $C_{k,10N}$ curves that level off and then rise at very high wind speeds.

It is important to note that heat fluxes with spray in this study were diagnosed from UWIN-CM output rather than calculated within the coupled simulations themselves. When spray heat fluxes are allowed to interact with the resolved-scale AWO system, they will modify resolved-scale properties, creating feedbacks that may either dampen or amplify the spray heat fluxes (e.g., large spray LHF will increase $q$ and $s$ at the LML, creating a feedback that diminishes the spray LHF). For simplicity, we have chosen to limit this study's

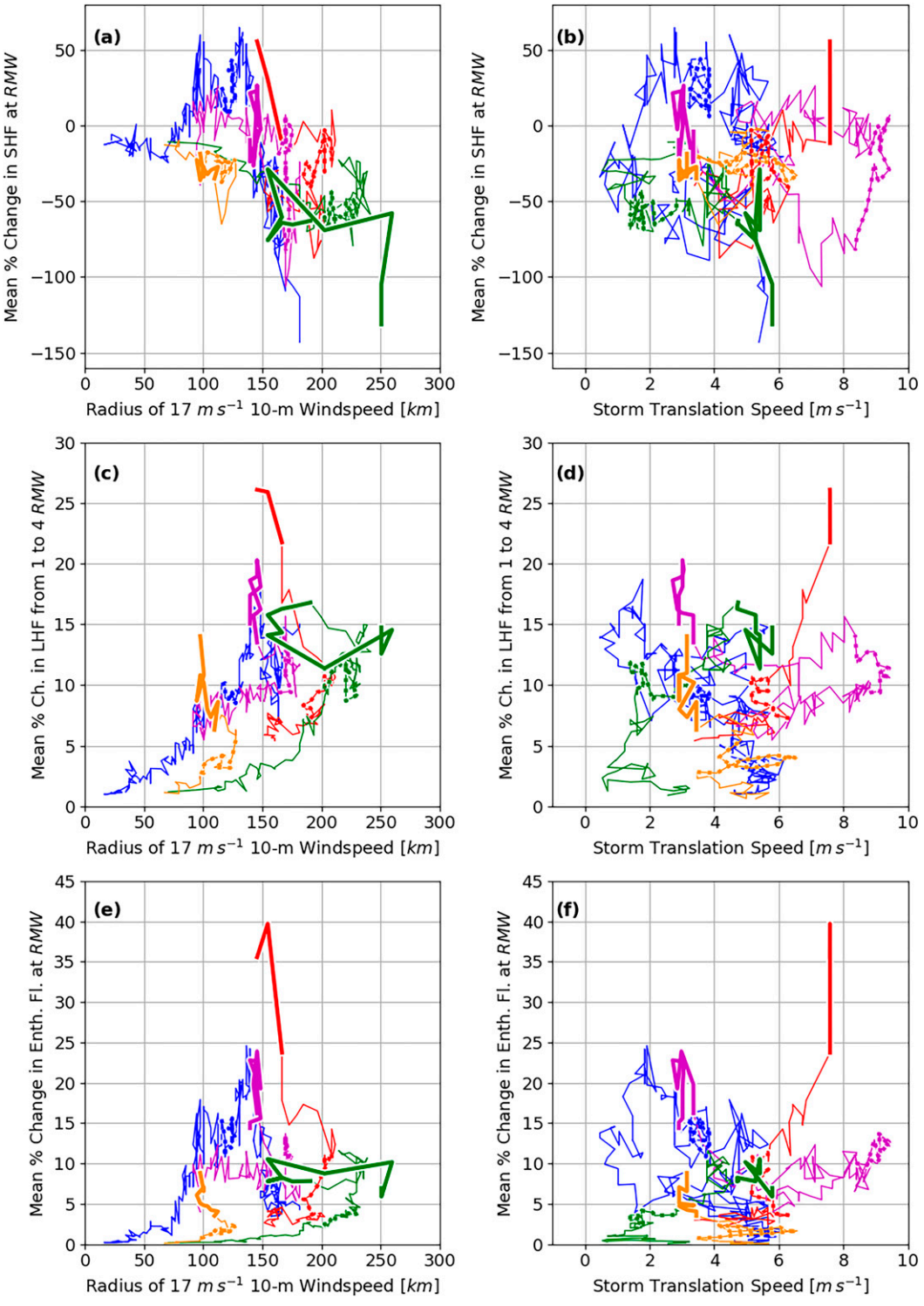


FIG. 15. Time traces of metrics for spray through the full simulation time period for all storms (calculations performed hourly). (a),(b) Mean percentage change in SHF due to spray at the RMW, (c),(d) mean percentage change in LHF due to spray between 1 and 4RMW, and (e),(f) mean percentage change in enthalpy flux due to spray at the RMW. (a), (c), and (e) are plotted vs the radius of 17 m $s^{-1}$ (gale force) azimuthal-mean 10-m wind speed, and (b), (d), and (f) are plotted vs storm translational speed. Line styles and colors are as in Fig. 14.

scope to diagnosing heat fluxes from coupled model output only; all considerations related to coupled interactions between spray and the AWO system, including feedbacks between spray and the resolved-scale environment at the air–sea interface, are left for future work.

The new parameterization contains a number of parameters that are poorly understood and that would benefit from additional observational and modeling work. Spray generation remains poorly observed, especially in high-wind field conditions, and experimental and modeling work targeting the dynamics of droplet generation at wave crests and entrainment of droplets into the turbulent near-surface flow could help calibrate our sea-state-based SSGF or determine if more suitable scalings exist than those currently used. Our model predicts that droplet cooling and evaporation are most efficient for droplets with $r_0$ near 300 and 20 $\mu$m, respectively (Figs. 5c,d), suggesting that these droplet sizes should be targeted when designing future observational studies on spray generation. Mueller and Veron (2014a) have shown that the droplet residence time is more complex than as assumed in (8); additional numerical work (e.g., large-eddy simulations) studying droplet transport across complex seas (including those with swell and misaligned wind and waves) would be helpful in calibrating our model. Finally, our model's assumption of uniform vertical heating within the spray layer when calculating near-surface feedback (A10) is likely an oversimplification, and the model would benefit from numerical work investigating the vertical distribution of spray heat flux into the spray layer for a wide range of droplet sizes and sea states.

Despite the uncertainty in our new parameterization, we believe that this study's results indicate strong control of spray effects by wave processes and demonstrate that explicit representation of sea-state-based spray generation and heat transfer in high-wind air–sea heat flux calculations is essential. The new parameterization has been implemented in UWIN-CM, and analysis is underway to examine the coupled interactive processes between waves, spray heat fluxes, the atmospheric surface and boundary layers, and the TC vortex, including 1) feedback between spray heat fluxes and the resolved-scale environment at the air–sea interface, 2) the impact of spray moistening/cooling effects on stability and inflow outside the eyewall, and 3) the impact of spray on eyewall convection.

We hope that this study and related work will facilitate inclusion of spray physics in operation hurricane forecast models. Toward this goal, we emphasize the importance of the SSGF in driving all spray effects and recognize the challenge of implementing sea-state-dependent spray physics in operational models, which requires coupling to a wave model with sufficient resolution to resolve the relevant wave field characteristics. We hope that continued development of parameterizations like the one presented herein and of computationally efficient, coupling-friendly wave models like the UMWM will help realize the goal of fully coupled AWO operational model forecasts of TC intensity and impacts.

*Acknowledgments.* This research is supported in part by the NASA MAP Grant 80NSSC17K0421, the NSF Grant OCE-1756412, and the Gulf of Mexico Research Initiative Grant SA 18-14 (Subaward SPC-000581 AM 1). B. W. Barr is supported by NASA Future Investigators in NASA Earth and Space Science and Technology (FINESST) Award 80NSSC19 K1336. The authors thank Brandon Kerns, Milan Curcic, Edoardo Mazza, and Dalton Sasaki for their contributions to the UWIN-CM simulations used in this study. The authors also thank three anonymous reviewers for their thoughtful and constructive review comments on the manuscript, which helped improve the manuscript significantly.

*Data availability statement.* Coupled model output, spray calculation fields, and further information about the new parameterization and its implementation in AWO models can be obtained upon request to Benjamin Barr (bwbarr@uw.edu).

## APPENDIX

### Additional Details for Air–Sea Heat Flux Parameterization with Spray

#### *a. Spray generation*

Additional details defining variables in section 3a and a summary of the sea-state-based SSGF calibration process follow. We define $W_{SS}$ based on Deike et al. (2017) as follows:

$$W_{SS} = (0.018\,\mathrm{s\,m^{-1}})\frac{C_{p,d}u_*^2}{gH_S}, \tag{A1}$$

where $g$ is the acceleration due to gravity. We define $W_{wi}$ using a simple wind speed fit to the formula given as Eq. (12) in Blomquist et al. (2017):

$$W_{wi} = (6.5\times10^{-4}\ \mathrm{s^{1.5}\,m^{-1.5}})(U_{10} - 2\,\mathrm{m\,s^{-1}})^{1.5}; \tag{A2}$$

$\eta_k$ is defined in the usual way as $\eta_k = (\nu_{sw}^3/\tilde{\varepsilon})^{1/4}$, with $\nu_{sw}$ as the kinematic viscosity of seawater. Note that $\eta_k$ depends on $W_{SS}$ through $\tilde{\varepsilon}$.

The argument of the error function in (1) without tuning coefficients is $(U_{h,\mathrm{rel}} - v_g/s_m)/\sigma_h$ and represents a comparison between the ballistics of droplets at the wave crest (numerator) and the strength of the gusts that entrain them into the surface flow (denominator). The numerator relates the slope of a droplet's wave-relative trajectory off the crest ($-v_g/U_{h,\mathrm{rel}}$, assuming constant horizontal and vertical speeds $U_{h,\mathrm{rel}}$ and $v_g$, respectively) to the slope of the underlying wave face ($-s_m$). We assume that droplets instantly accelerate to the local horizontal wind speed $U_h$ as they exit the wave crest, so that $U_{h,\mathrm{rel}} = U_h - 0.8C_{p,d}$. In this simple model, the wind properties $U_h$ and $\sigma_h$ should be extracted at a characteristic height for the ejection/entrainment process, which is the gust height $h_{\mathrm{gust}}$. We define $h_{\mathrm{gust}}$ herein as $200z_0$, where $z_0$ is the momentum roughness length and the factor of 200 is chosen based on additional analysis so that $U_{h,\mathrm{rel}}$ will be positive for $U_{10} \gtrsim 25\,\mathrm{m\,s^{-1}}$ (i.e., when spray effects become prevalent). We note that the dynamics encapsulated in the error function argument are highly uncertain and would benefit from targeted experimental and numerical studies.

$v_g$ is defined per Pruppacher and Klett (1997). $\sigma_h$ is not available from WRF and is parameterized as being proportional to $U_{10}$ [similar to the code accompanying C. W. Fairall et al. (2014, unpublished report)], with the constant of proportionality absorbed into $C_4$. All wind speeds and $z_0$ are calculated per standard MO theory using $u_*$ and $U_1$.

Our sea-state-based SSGF was calibrated using the laboratory results of OS16 and the F94 SSGF droplet spectrum shape. The OS16 results [their Fig. 11a and Eq. (23)] cover $80 \lesssim r_0 \lesssim 2000\,\mu$m, which includes the SSGF peak and large droplet tail but not the small droplet tail. The F94 spectrum's small droplet tail ($2 \lesssim r_0 \lesssim 30\,\mu$m) is based on data from Miller (1987). Its large droplet tail and peak ($30 \lesssim r_0 \lesssim 500\,\mu$m), which does not move to higher $r_0$ as $U_{10}$ increases, is based on data from Wu et al. (1984).

We calibrated model coefficients $C_1$ and $C_2$, which control the spectrum magnitude and small droplet tail, to the Miller (1987) portion of the F94 spectrum. We calibrated $C_3$, $C_4$, and $C_5$, which control the peak and large-droplet tail, to the OS16 results. The five coefficients were calibrated simultaneously by fitting one set of coefficients (e.g., $C_3$, $C_4$, $C_5$) to its relevant dataset (e.g., OS16) using least squares minimization while holding the other set of coefficients (e.g., $C_1$, $C_2$) constant, then repeating the process with updated coefficients for the other dataset (e.g., F94), and switching back and forth until all coefficients converged. The converged values of the coefficients are $C_1 = 1.92$, $C_2 = 0.1116$, $C_3 = 0.719$, $C_4 = 2.17$, and $C_5 = 0.852$.

We then used $f_s$ to calibrate the total mass flux for our sea-state-based and wind-based SSGFs using the F94 SSGF with its original whitecap formulation (Monahan and O'Muircheartaigh 1980). Based on unpublished spray observations from E. L. Andreas (1993, private communication) and the original Andreas (1992) model, the original F94 SSGF is considered to predict reasonable spray mass flux at $U_{10} = 30$ m s$^{-1}$ when $f_s = 0.4$. Tuning our updated wind-based SSGF to match this gives $f_s = 2.2$. For simplicity, we chose to assign $f_s = 2.2$ to our sea-state-based SSGF as well, which required an adjustment of $C_1$ to 1.35. Note that $C_1$ and $f_s$ could be combined in the sea-state-based model. $f_s$ is the "sourcestrength" parameter used in various codes (e.g., C. W. Fairall et al. 2014, unpublished report) to scale the spray mass flux and is retained for historical consistency. Forcing $f_s = 2.2$ in both our sea-state-based and updated wind-based SSGFs simplifies future adjustment of both as more observations become available.

### b. Spray heat fluxes

Additional details defining variables in section 3b follow. We define the salt-adjusted wet-bulb depression $\Delta T_{\rm wb} = T - T_{\rm wb}$ and the wet-bulb coefficient $\beta$ per classical thermodynamics (e.g., F94; Pruppacher and Klett 1997) as follows:

$$\Delta T_{\rm wb} = \frac{\left(1 - \dfrac{s}{1 + y_0}\right)(1 - \beta)}{\gamma} \tag{A3a}$$

$$\beta = \left[1 + \frac{L_v \gamma (1 + y_0)}{c_{p,a}} q_{\rm sat,0}(T)\right]^{-1}. \tag{A3b}$$

Here $\gamma = [dq_{\rm sat,0}(\tilde{T})/d\tilde{T}|_T]/q_{\rm sat,0}(T)$.

The parameter $y_0$ is defined as

$$y_0 = -\frac{\nu \Phi_s \dfrac{M_w}{M_s} x_s}{1 - x_s}. \tag{A4}$$

Finally, it is common to extract ambient conditions ($T$, $q$) for spray calculations at a height related to spray-layer geometry (e.g., $\delta$ in F94). However, Mueller and Veron (2014a) and Peng and Richter (2019) showed that this scaling is not appropriate for small droplets, which respond quickly to local conditions and can reheat or regrow by condensation as they reenter the ocean. We account for small droplet reheating and regrowth following Peng and Richter (2019) by specifying radius-specific heights $z_T$ and $z_R$ for use in $H_{T,\rm spr}$ and $H_{R,\rm spr}$ calculations, respectively, as follows:

$$z_T(r_0) = 0.5 \min(\delta, v_g \tau_T), \tag{A5a}$$

$$z_R(r_0) = 0.5 \min(\delta, v_g \tau_R). \tag{A5b}$$

### c. Air–sea heat fluxes with spray and near-surface feedback

In this section, we derive the model for heat transfer within a MO surface layer with spray heating discussed in section 3c.

Using first-order closure with a mixing length model for eddy diffusivity, the vertical turbulent sensible heat ($H_S$) and latent heat ($H_L$) fluxes as a function of height $z$ are

$$H_S(z) = -\rho_a c_{p,a} \frac{\kappa u_* z}{\phi_H(\zeta)} \frac{d\theta}{dz}, \tag{A6a}$$

$$H_L(z) = -\rho_a L_v \frac{\kappa u_* z}{\phi_H(\zeta)} \frac{dq}{dz}. \tag{A6b}$$

Here $\phi_H$ is the universal stability function for heat, which depends on the stability parameter $\zeta = z/L$, with $L$ the Obukhov stability length. When spray is absent, these turbulent fluxes are assumed constant with height, and (A6) can be integrated to obtain the turbulent interfacial sensible and latent heat fluxes, $H_S'$ and $H_L'$ (17). We do not address spray impacts on stability herein and therefore define $L$ in terms of heat fluxes without spray (i.e., $H_S'$ and $H_L'$) as follows:

$$L = \frac{u_*^2}{\kappa \left(\dfrac{g}{\theta_1}\right)\left(-\dfrac{H_S'}{\rho_a c_{p,a} u_*} - 0.61 \theta_1 \dfrac{H_L'}{\rho_a L_v u_*}\right)}. \tag{A7}$$

When spray is present, it carries part of the total heat fluxes, so that there is an apparent vertical divergence of the turbulent heat fluxes:

$$\frac{dH_S}{dz} = \hat{H}_S(z), \tag{A8a}$$

$$\frac{dH_L}{dz} = \hat{H}_L(z). \tag{A8b}$$

Here $\hat{H}_S$ and $\hat{H}_L$ are height-dependent volumetric sources of sensible and latent heat, respectively, due to heat transfer from spray droplets to the surface layer. Plugging (A6) into (A8) and integrating twice from $z_{0t}$ and $z_{0q}$ to an arbitrary height $z$ gives

$$\rho_a c_{p,a} \kappa u_* (\theta_0 - \theta) = H_{S,0}\left[\ln\left(\frac{z}{z_{0t}}\right) - \Psi_H(\zeta)\right] + \int_{z_{0t}}^{z} \frac{\phi_H(\tilde{\tilde{z}}/L)}{\tilde{\tilde{z}}} \int_{z_{0t}}^{\tilde{\tilde{z}}} \hat{H}_S(\tilde{z}) d\tilde{z}\, d\tilde{\tilde{z}}, \tag{A9a}$$

$$\rho_a L_v \kappa u_* (q_0 - q) = H_{L,0}\left[\ln\left(\frac{z}{z_{0q}}\right) - \Psi_H(\zeta)\right] + \int_{z_{0q}}^{z} \frac{\phi_H(\tilde{\tilde{z}}/L)}{\tilde{\tilde{z}}} \int_{z_{0q}}^{\tilde{\tilde{z}}} \hat{H}_L(\tilde{z}) d\tilde{z}\, d\tilde{\tilde{z}}. \tag{A9b}$$

Here $H_{S,0}$ and $H_{L,0}$ are the heat fluxes at the surface, including spray effects. In (A9) and the remaining derivation, we neglect small terms involving $z_{0t}$ or $z_{0q}$, such as $\Psi_H(z_{0t}/L)$.

Kepert et al. (1999) and Bianco et al. (2011) suggest that volumetric heating due to spray is negligible above the spray layer. Similar to Smith (1990), Andreas et al. (1995), and C. W. Fairall et al. (2014, unpublished report), we assume that spray heats the spray layer uniformly, so that

$$\hat{H}_S(z) = \begin{cases} \frac{1}{\delta} H_{\mathrm{SN,spr}} & z \le \delta \\ 0 & z > \delta \end{cases}, \tag{A10a}$$

$$\hat{H}_L(z) = \begin{cases} \frac{1}{\delta} H_{L,\mathrm{spr}} & z \le \delta \\ 0 & z > \delta \end{cases}. \tag{A10b}$$

Plugging (A10) into (A9) and integrating twice, we obtain the $\theta$ and $q$ profiles within the spray layer:

$$\rho_a c_{p,a} \kappa u_* (\theta_0 - \theta) = H_{S,0}\left[\ln\left(\frac{z}{z_{0t}}\right) - \Psi_H(\zeta)\right] + \frac{z}{\delta} H_{\mathrm{SN,spr}}[1 - \varphi_H(\zeta)], \tag{A11a}$$

$$\rho_a L_v \kappa u_* (q_0 - q) = H_{L,0}\left[\ln\left(\frac{z}{z_{0q}}\right) - \Psi_H(\zeta)\right] + \frac{z}{\delta} H_{L,\mathrm{spr}}[1 - \varphi_H(\zeta)]; \tag{A11b}$$

$\varphi_H(\zeta)$ is the analog of $\Psi_H(\zeta)$ for a layer with volumetric heating. Using the standard prescription for $\phi_H$ (Paulson 1970; Webb 1970; Dyer 1974), $\varphi_H(\zeta)$ is

$$\varphi_H(\zeta) = -\frac{[(1 - 16\zeta)^{1/2} - 1]^2}{16\zeta}, \quad \zeta < 0, \tag{A12a}$$

$$\varphi_H(\zeta) = 0, \quad \zeta = 0, \tag{A12b}$$

$$\varphi_H(\zeta) = -2.5\zeta, \quad \zeta > 0. \tag{A12c}$$

We recognize in (A11) the standard log layer and stability terms as well as new terms contributed by spray.

The region between $z = \delta$ and $z_1$ is governed by the standard log law. Enforcing continuity of $\theta$, $q$, and flux at $z = \delta$, we can solve for $H_{S,1}$ and $H_{L,1}$, which are (16). We can also solve for the fluxes at the surface, $H_{S,0}$ and $H_{L,0}$, which are

$$H_{S,0} = H'_S - (1 - \gamma_S)(H_{S,\mathrm{spr}} - H_{R,\mathrm{spr}}), \tag{A13a}$$

$$H_{L,0} = H'_L - (1 - \gamma_L) H_{L,\mathrm{spr}}. \tag{A13b}$$

Finally, we briefly compare the physics of our near-surface feedback model to three other prominent published approaches (Andreas et al. 2015; Bao et al. 2011; Mueller and Veron 2014b).

Andreas et al. (2015) address feedback by applying tuning coefficients to their spray heat fluxes. These coefficients are determined empirically based on numerous datasets and do not directly deal with physical processes in the surface layer.

Bao et al. (2011) address feedback in a physics-based way by estimating changes to temperature and humidity due to spray heat fluxes that would occur in a thermodynamically lumped column of air extending from the surface to the lowest atmospheric model level, accounting for conservation of enthalpy by evaporating spray droplets. These changes are then applied as perturbations to the temperature and humidity potentials used to calculate turbulent and spray heat fluxes. Our approach differs from this in that we directly calculate the full spray-modified temperature and humidity profiles in the surface layer, rather than lumped estimates of their changes, for use in heat flux calculations. Additionally, our calculation of full modified profiles directly yields the heat fluxes with spray applied to the atmospheric model, (16).

Mueller and Veron (2014b) calculate spray-modified profiles of temperature and humidity in the surface layer and use these to calculate heat fluxes with near-surface feedback, making their approach to feedback similar to ours, although with a different derivation and final form for the total heat flux expressions. However, their model and ours take different approaches on several important and challenging modeling issues, including specifying the vertical distribution of spray heat fluxes in the surface layer, determining droplet reentry temperature and size, and modeling sea-state-dependent spray generation.

## REFERENCES

Andreas, E. L., 1989: Thermal and size evolution of sea spray droplets. CRREL Rep. 89-11, 38 pp., https://apps.dtic.mil/sti/pdfs/ADA210484.pdf.

——, 1990: Time constants for the evolution of sea spray droplets. *Tellus*, **42B**, 481–497, https://doi.org/10.3402/tellusb.v42i5.15241.
——, 1992: Sea spray and the turbulent air-sea heat fluxes. *J. Geophys. Res.*, **97**, 11 429–11 441, https://doi.org/10.1029/92JC00876.
——, 2004: Spray stress revisited. *J. Phys. Oceanogr.*, **34**, 1429–1440, https://doi.org/10.1175/1520-0485(2004)034<1429:SSR>2.0.CO;2.
——, 2005: Approximation formulas for the microphysical properties of saline droplets. *Atmos. Res.*, **75**, 323–345, https://doi.org/10.1016/j.atmosres.2005.02.001.
——, and J. DeCosmo, 1999: Sea spray production and influence on air-sea heat and moisture fluxes over the open ocean. *Air-Sea Exchange: Physics, Chemistry and Dynamics*, G. L. Geernaert, Ed., Kluwer, 327–362.
——, and K. A. Emanuel, 2001: Effects of sea spray on tropical cyclone intensity. *J. Atmos. Sci.*, **58**, 3741–3751, https://doi.org/10.1175/1520-0469(2001)058<3741:EOSSOT>2.0.CO;2.
——, J. B. Edson, E. C. Monahan, M. P. Rouault, and S. D. Smith, 1995: The spray contribution to net evaporation from the sea: A review of recent progress. *Bound.-Layer Meteor.*, **72**, 3–52, https://doi.org/10.1007/BF00712389.
——, L. Mahrt, and D. Vickers, 2015: An improved bulk air–sea surface flux algorithm, including spray-mediated transfer. *Quart. J. Roy. Meteor. Soc.*, **141**, 642–654, https://doi.org/10.1002/qj.2424.
Avila, L. A., S. R. Stewart, R. Berg, and A. B. Hagen, 2020: National Hurricane Center tropical cyclone report: Hurricane Dorian. NHC Tech. Rep. AL052019, 74 pp., https://www.nhc.noaa.gov/data/tcr/AL052019_Dorian.pdf.
Banner, M. L., X. Barthelemy, F. Fedele, M. Allis, A. Benetazzo, F. Dias, and W. L. Peirson, 2014: Linking reduced breaking crest speeds to unsteady nonlinear water wave group behavior. *Phys. Rev. Lett.*, **112**, 114502, https://doi.org/10.1103/PhysRevLett.112.114502.
Bao, J.-W., J. M. Wilczak, J.-K. Choi, and L. H. Kantha, 2000: Numerical simulations of air–sea interaction under high wind conditions using a coupled model: A study of hurricane development. *Mon. Wea. Rev.*, **128**, 2190–2210, https://doi.org/10.1175/1520-0493(2000)128<2190:NSOASI>2.0.CO;2.
——, C. W. Fairall, S. A. Michelson, and L. Bianco, 2011: Parameterizations of sea-spray impact on the air–sea momentum and heat fluxes. *Mon. Wea. Rev.*, **139**, 3781–3797, https://doi.org/10.1175/MWR-D-11-00007.1.
Bianco, L., J.-W. Bao, C. W. Fairall, and S. A. Michelson, 2011: Impact of sea-spray on the atmospheric surface layer. *Bound.-Layer Meteor.*, **140**, 361–381, https://doi.org/10.1007/s10546-011-9617-1.
Blomquist, B. W., and Coauthors, 2017: Wind speed and sea state dependencies of air-sea gas transfer: Results from the High Wind Speed Gas Exchange Study (HiWinGS). *J. Geophys. Res. Oceans*, **122**, 8034–8062, https://doi.org/10.1002/2017JC013181.
Bruch, W., J. Piazzola, H. Branger, A. M. J. van Eijk, C. Luneau, D. Bourras, and G. Tedeschi, 2021: Sea-spray-generation dependence on wind and wave combinations: A laboratory study. *Bound.-Layer Meteor.*, **180**, 477–505, https://doi.org/10.1007/s10546-021-00636-y.
Brumer, S. E., C. J. Zappa, I. M. Brooks, H. Tamura, S. M. Brown, B. W. Blomquist, C. W. Fairall, and A. Cifuentes-Lorenzen, 2017: Whitecap coverage dependence on wind and wave statistics as observed during SO GasEX and HiWinGS. *J. Phys. Oceanogr.*, **47**, 2211–2235, https://doi.org/10.1175/JPO-D-17-0005.1.
Cangialosi, J. P., 2020: National Hurricane Center forecast verification report: 2019 hurricane season. National Hurricane Center Rep., 75 pp.
Chen, S. S., and M. Curcic, 2016: Ocean surface waves in Hurricane Ike (2008) and Superstorm Sandy (2012): Coupled model predictions and observations. *Ocean Modell.*, **103**, 161–176, https://doi.org/10.1016/j.ocemod.2015.08.005.
——, J. F. Price, W. Zhao, M. A. Donelan, and E. J. Walsh, 2007: The CBLAST-Hurricane Program and the next-generation fully coupled atmosphere–wave–ocean models for hurricane research and prediction. *Bull. Amer. Meteor. Soc.*, **88**, 311–317, https://doi.org/10.1175/BAMS-88-3-311.
——, W. Zhao, M. A. Donelan, and H. L. Tolman, 2013: Directional wind–wave coupling in fully coupled atmosphere–wave–ocean models: Results from CBLAST-Hurricane. *J. Atmos. Sci.*, **70**, 3198–3215, https://doi.org/10.1175/JAS-D-12-0157.1.
Cheng, X., J. Fei, X. Huang, and J. Zheng, 2012: Effects of sea spray evaporation and dissipative heating on intensity and structure of tropical cyclone. *Adv. Atmos. Sci.*, **29**, 810–822, https://doi.org/10.1007/s00376-012-1082-3.
Deike, L., L. Lenain, and W. K. Melville, 2017: Air entrainment by breaking waves. *Geophys. Res. Lett.*, **44**, 3779–3787, https://doi.org/10.1002/2017GL072883.
Donelan, M. A., M. Curcic, S. S. Chen, and A. K. Magnusson, 2012: Modeling waves and wind stress. *J. Geophys. Res.*, **117**, C00J23, https://doi.org/10.1029/2011JC007787.
Drennan, W. M., J. A. Zhang, J. R. French, C. McCormick, and P. G. Black, 2007: Turbulent fluxes in the hurricane boundary layer. Part II: Latent heat flux. *J. Atmos. Sci.*, **64**, 1103–1115, https://doi.org/10.1175/JAS3889.1.
Dyer, A. J., 1974: A review of flux-profile relationships. *Bound.-Layer Meteor.*, **7**, 363–372, https://doi.org/10.1007/BF00240838.
Emanuel, K. A., 1995: Sensitivity of tropical cyclones to surface exchange coefficients and a revised steady-state model incorporating eye dynamics. *J. Atmos. Sci.*, **52**, 3969–3976, https://doi.org/10.1175/1520-0469(1995)052<3969:SOTCTS>2.0.CO;2.
Fairall, C. W., J. B. Edson, and M. A. Miller, 1990: Heat fluxes, whitecaps, and sea spray. *Current Theory*, G. L. Geernaert, Ed., Vol. I, *Surface Waves and Fluxes*, Kluwer, 173–208.
——, J. D. Kepert, and G. J. Holland, 1994: The effect of sea spray on surface energy transports over the ocean. *Global Atmos. Ocean Syst.*, **2**, 121–142.
——, E. F. Bradley, J. E. Hare, A. A. Grachev, and J. B. Edson, 2003: Bulk parameterization of air–sea fluxes: Updates and verification for the COARE algorithm. *J. Climate*, **16**, 571–591, https://doi.org/10.1175/1520-0442(2003)016<0571:BPOASF>2.0.CO;2.
——, M. L. Banner, W. L. Peirson, W. Asher, and R. P. Morison, 2009: Investigation of the physical scaling of sea spray spume droplet production. *J. Geophys. Res.*, **114**, C10001, https://doi.org/10.1029/2008JC004918.
Figa-Saldaña, J., J. J. W. Wilson, E. Attema, R. Gelsthorpe, M. R. Drinkwater, and A. Stoffelen, 2002: The Advanced Scatterometer (ASCAT) on the Meteorological Operational (MetOp) platform: A follow on for European wind scatterometers. *Can. J. Remote Sens.*, **28**, 404–412, https://doi.org/10.5589/m02-035.
Garg, N., E. Y. K. Ng, and S. Narasimalu, 2018: The effects of sea spray and atmosphere–wave coupling on air–sea exchange during a tropical cyclone. *Atmos. Chem. Phys.*, **18**, 6001–6021, https://doi.org/10.5194/acp-18-6001-2018.
Garratt, J. R., 1992: *The Atmospheric Boundary Layer*. Cambridge University Press, 316 pp.

He, H., Q. Wu, D. Chen, J. Sun, C. Liang, W. Jin, and Y. Xu, 2018: Effects of surface waves and sea spray on air–sea fluxes during the passage of Typhoon Hagupit. *Acta Oceanol. Sin.*, **37** (5), 1–7, https://doi.org/10.1007/s13131-018-1208-2.

Hong, S.-Y., Y. Noh, and J. Dudhia, 2006: A new vertical diffusion package with an explicit treatment of entrainment processes. *Mon. Wea. Rev.*, **134**, 2318–2341, https://doi.org/10.1175/MWR3199.1.

Kepert, J., C. W. Fairall, and J.-W. Bao, 1999: Modelling the interaction between the atmospheric boundary layer and evaporating sea spray droplets. *Air-Sea Exchange: Physics, Chemistry and Dynamics*, G. L. Geernaert, Ed., Kluwer, 363–409.

Lee, C.-Y., and S. S. Chen, 2014: Stable boundary layer and its impact on tropical cyclone structure in a coupled atmosphere–ocean model. *Mon. Wea. Rev.*, **142**, 1927–1944, https://doi.org/10.1175/MWR-D-13-00122.1.

Lin, K.-L., S.-C. Yang, and S. S. Chen, 2018: Reducing TC position uncertainty in ensemble data assimilation and prediction system: A case study of Typhoon Fanapi (2010). *Wea. Forecasting*, **33**, 561–582, https://doi.org/10.1175/WAF-D-17-0152.1.

Miller, M. A., 1987: An investigation of aerosol generation in the marine planetary boundary layer. M.S. thesis, Dept. of Meteorology, Pennsylvania State University, 142 pp.

Monahan, E. C., and I. O'Muircheartaigh, 1980: Optimal power-law description of oceanic whitecap coverage dependence on wind speed. *J. Phys. Oceanogr.*, **10**, 2094–2099, https://doi.org/10.1175/1520-0485(1980)010<2094:OPLDOO>2.0.CO;2.

——, D. E. Spiel, and K. L. Davidson, 1986: A model of marine aerosol generation via whitecaps and wave disruption. *Oceanic Whitecaps*, E. C. Monahan and G. Niocaill, Eds., Springer, 167–174.

Monin, A. S., and A. M. Obukhov, 1954: Basic laws of turbulent mixing in the atmosphere near the ground. *Tr. Geofiz. Inst., Akad. Nauk SSSR*, **24**, 163–187.

Mueller, J. A., and F. Veron, 2009: A sea state–dependent spume generation function. *J. Phys. Oceanogr.*, **39**, 2363–2372, https://doi.org/10.1175/2009JPO4113.1.

——, and ——, 2014a: Impact of sea spray on air–sea fluxes. Part I: Results from stochastic simulations of sea spray drops over the ocean. *J. Phys. Oceanogr.*, **44**, 2817–2834, https://doi.org/10.1175/JPO-D-13-0245.1.

——, and ——, 2014b: Impact of sea spray on air–sea fluxes. Part II: Feedback effects. *J. Phys. Oceanogr.*, **44**, 2835–2853, https://doi.org/10.1175/JPO-D-13-0246.1.

Ortiz-Suslow, D. G., B. K. Haus, S. Mehta, and N. J. M. Laxague, 2016: Sea spray generation in very high winds. *J. Atmos. Sci.*, **73**, 3975–3995, https://doi.org/10.1175/JAS-D-15-0249.1.

Paulson, C. A., 1970: The mathematical representation of wind speed and temperature profiles in the unstable atmospheric surface layer. *J. Appl. Meteor. Climatol.*, **9**, 857–861, https://doi.org/10.1175/1520-0450(1970)009<0857:TMROWS>2.0.CO;2.

Peng, T., and D. H. Richter, 2019: Sea spray and its feedback effects: Assessing bulk algorithms of air–sea heat fluxes via direct numerical simulations. *J. Phys. Oceanogr.*, **49**, 1403–1421, https://doi.org/10.1175/JPO-D-18-0193.1.

Prakash, K. R., V. Pant, and T. Nigam, 2019: Effects of the sea surface roughness and sea spray-induced flux parameterization on the simulations of a tropical cyclone. *J. Geophys. Res. Atmos.*, **124**, 14 037–14 058, https://doi.org/10.1029/2018JD029760.

Price, J. F., 1981: Upper ocean response to a hurricane. *J. Phys. Oceanogr.*, **11**, 153–175, https://doi.org/10.1175/1520-0485(1981)011<0153:UORTAH>2.0.CO;2.

Pruppacher, H. R., and J. D. Klett, 1997: *Microphysics of Clouds and Precipitation*. 2nd ed. Kluwer Academic, 954 pp.

Remote Sensing Systems, 2017: MWIR optimum interpolated SST dataset, version 5.0. PO.DAAC, accessed 11 February 2021, https://doi.org/10.5067/GHMWI-4FR05.

Richter, D. H., and D. P. Stern, 2014: Evidence of spray-mediated air-sea enthalpy flux within tropical cyclones. *Geophys. Res. Lett.*, **41**, 2997–3003, https://doi.org/10.1002/2014GL059746.

——, and F. Veron, 2016: Ocean spray: An outsized influence on weather and climate. *Phys. Today*, **69**, 34–39, https://doi.org/10.1063/PT.3.3363.

Shapiro, L. J., 1983: The asymmetric boundary layer flow under a translating hurricane. *J. Atmos. Sci.*, **40**, 1984–1998, https://doi.org/10.1175/1520-0469(1983)040<1984:TABLFU>2.0.CO;2.

——, and H. E. Willoughby, 1982: The response of balanced hurricanes to local sources of heat and momentum. *J. Atmos. Sci.*, **39**, 378–394, https://doi.org/10.1175/1520-0469(1982)039<0378:TROBHT>2.0.CO;2.

Shpund, J., J. A. Zhang, M. Pinsky, and A. Khain, 2012: Microphysical structure of the marine boundary layer under strong wind and spray formation as seen from simulations using a 2D explicit microphysical model. Part II: The role of sea spray. *J. Atmos. Sci.*, **69**, 3501–3514, https://doi.org/10.1175/JAS-D-11-0281.1.

Skamarock, W. C., and Coauthors, 2008: A description of the Advanced Research WRF version 3. NCAR Tech. Note NCAR/TN-475+STR, 113 pp., https://doi.org/10.5065/D68S4MVH.

Smith, S. D., 1990: Influence of droplet evaporation on HEXOS humidity and temperature profiles. Modeling the fate and influence of marine spray, University of Connecticut Marine Sciences Institute Whitecap Rep. 7, 171–174.

Sroka, S., and K. A. Emanuel, 2021a: A review of parameterizations for enthalpy and momentum fluxes from sea spray in tropical cyclones. *J. Phys. Oceanogr.*, **51**, 3053–3069, https://doi.org/10.1175/JPO-D-21-0023.1.

——, and ——, 2021b: Sensitivity of sea-surface enthalpy and momentum fluxes to sea spray microphysics. *J. Geophys. Res. Oceans*, **127**, e2021JC017774, https://doi.org/10.1029/2021JC017774.

Sutherland, P., and W. K. Melville, 2015: Field measurements of surface and near-surface turbulence in the presence of breaking waves. *J. Phys. Oceanogr.*, **45**, 943–965, https://doi.org/10.1175/JPO-D-14-0133.1.

Tamizi, A., and I. R. Young, 2020: The spatial distribution of ocean waves in tropical cyclones. *J. Phys. Oceanogr.*, **50**, 2123–2139, https://doi.org/10.1175/JPO-D-20-0020.1.

Troitskaya, Y., A. Kandaurov, O. Ermakova, D. Kozlov, D. Sergeev, and S. Zilitinkevich, 2017: Bag-breakup fragmentation as the dominant mechanism of sea-spray production in high winds. *Sci. Rep.*, **7**, 1614, https://doi.org/10.1038/s41598-017-01673-9.

——, ——, ——, ——, ——, and ——, 2018a: The "bag breakup" spume droplet generation mechanism at high winds. Part I: Spray generation function. *J. Phys. Oceanogr.*, **48**, 2167–2188, https://doi.org/10.1175/JPO-D-17-0104.1.

——, O. Druzhinin, D. Kozlov, and S. Zilitinkevich, 2018b: The "bag breakup" spume droplet generation mechanism at high winds. Part II: Contribution to momentum and enthalpy transfer. *J. Phys. Oceanogr.*, **48**, 2189–2207, https://doi.org/10.1175/JPO-D-17-0105.1.

Uhlhorn, E. W., and P. G. Black, 2003: Verification of remotely sensed sea surface winds in hurricanes. *J. Atmos. Oceanic Technol.*, **20**, 99–116, https://doi.org/10.1175/1520-0426(2003)020<0099:VORSSS>2.0.CO;2.

——, ——, J. F. Franklin, M. Goodberlet, J. Carswell, and A. S. Goldstein, 2007: Hurricane surface wind measurements from an operational stepped-frequency microwave radiometer. *Mon. Wea. Rev.*, **135**, 3070–3085, https://doi.org/10.1175/MWR3454.1.

Veron, F., 2015: Ocean spray. *Annu. Rev. Fluid Mech.*, **47**, 507–538, https://doi.org/10.1146/annurev-fluid-010814-014651.

——, C. Hopkins, E. L. Harrison, and J. A. Mueller, 2012: Sea spray spume droplet production in high wind speeds. *Geophys. Res. Lett.*, **39**, L16602, https://doi.org/10.1029/2012GL052603.

Wallcraft, A. J., E. J. Metzger, and S. N. Carroll, 2009: Software design description for the Hybrid Coordinate Ocean Model (HYCOM) version 2.2. Naval Research Laboratory Tech. Rep. NRL/MR/732009-9166, 155 pp., https://apps.dtic.mil/sti/citations/ADA494779.

Wang, Y., J. D. Kepert, and G. J. Holland, 2001: The effect of sea spray evaporation on tropical cyclone boundary layer structure and intensity. *Mon. Wea. Rev.*, **129**, 2481–2500, https://doi.org/10.1175/1520-0493(2001)129<2481:TEOSSE>2.0.CO;2.

Webb, E. K., 1970: Profile relationships: The log-linear range, and extension to strong stability. *Quart. J. Roy. Meteor. Soc.*, **96**, 67–90, https://doi.org/10.1002/qj.49709640708.

Wright, C. W., and Coauthors, 2001: Hurricane directional wave spectrum spatial variation in the open ocean. *J. Phys. Oceanogr.*, **31**, 2472–2488, https://doi.org/10.1175/1520-0485(2001)031<2472:HDWSSV>2.0.CO;2.

Wu, J., J. J. Murray, and R. J. Lai, 1984: Production and distributions of sea spray. *J. Geophys. Res.*, **89**, 8163–8169, https://doi.org/10.1029/JC089iC05p08163.

Xu, X., J. J. Voermans, H. Ma, C. Guan, and A. V. Babanin, 2021a: A wind-wave-dependent sea spray volume flux model based on field experiments. *J. Mar. Sci. Eng.*, **9**, 1168, https://doi.org/10.3390/jmse9111168.

——, ——, Q. Liu, I.-J. Moon, C. Guan, and A. V. Babanin, 2021b: Impacts of the wave-dependent sea spray parameterizations on air–sea–wave coupled modeling under an idealized tropical cyclone. *J. Mar. Sci. Eng.*, **9**, 1390, https://doi.org/10.3390/jmse9121390.

Young, I. R., 1999: *Wind Generated Ocean Waves.* Elsevier Ocean Engineering Book Series, Vol. 2, Elsevier, 288 pp.

Zhang, J. A., P. G. Black, J. R. French, and W. M. Drennan, 2008: First direct measurements of enthalpy flux in the hurricane boundary layer: The CBLAST results. *Geophys. Res. Lett.*, **35**, L14813, https://doi.org/10.1029/2008GL034374.

Zhang, L., and L. Oey, 2019: An observational analysis of ocean surface waves in tropical cyclones in the western North Pacific Ocean. *J. Geophys. Res. Oceans*, **124**, 184–195, https://doi.org/10.1029/2018JC014517.

——, X. Zhang, P. C. Chu, C. Guan, H. Fu, G. Chao, G. Han, and W. Li, 2017: Impact of sea spray on the Yellow and East China Seas thermal structure during the passage of Typhoon Rammasun (2002). *J. Geophys. Res. Oceans*, **122**, 7783–7802, https://doi.org/10.1002/2016JC012592.

Zhao, D., Y. Toba, K. Sugioka, and S. Komori, 2006: New Sea spray generation function for spume droplets. *J. Geophys. Res.*, **111**, C02007, https://doi.org/10.1029/2005JC002960.